

# 1

---

## Space Radiation Effects in Electronics

---

**Luigi Dilillo<sup>1</sup>, Alexandre Bosser<sup>2</sup>, Arto Javanainen<sup>3,4</sup> and Ari Virtanen<sup>3</sup>**

<sup>1</sup>CNRS (Centre National De La Recherche Scientifique)/  
University of Montpellier/LIRMM (Laboratoire d’Informatique,  
de Robotique et de Microélectronique de Montpellier), France

<sup>2</sup>Space Technology Group, Department of Electronics and Nanoengineering,  
Aalto University, Finland

<sup>3</sup>Department of Physics, University of Jyväskylä, FI-40014 Jyväskylä,  
Finland

<sup>4</sup>Electrical Engineering and Computer Science Department,  
Vanderbilt University, Nashville, TN 37235, USA

“I am accepted in both sietch and village, young Master. But I am in  
His Majesty’s service, the Imperial Planetologist.”

Frank Herbert, Dune

### Abstract

This chapter introduces the topic of the effects of harsh radiation environments, first on electronic devices in general, and next on memory components, the case study of the book. Ionizing radiation is ubiquitous in space, in the form of charged particles, coming mainly from the Sun, supernovae explosions and other galaxies, and which can be trapped and concentrated by planetary magnetic fields. When striking electronic components, these energetic particles cause both cumulative and single-event (spontaneous) effects. The former induce a degradation in performance, such as increased leakage currents, which can eventually lead to the complete loss of device functionality. The latter are generally non-destructive, and in memory components, may induce bit flips. Electronic devices used in harsh radiation environments are almost systematically characterized with accelerated tests in irradiation

## 2 Space Radiation Effects in Electronics

facilities, which use radiation beams to reproduce the target environment. For space applications, single-event characterization is typically done using particle accelerators which provide heavy ions and/or protons.

### 1.1 Space Radiation Environment

In the vacuum of space, energetic particles can travel over great distances without energy loss. In outer space, away from any radiation sources (i.e. stars) and intense magnetic dipoles, the amount of particle radiation is very small. However, in proximity of the Sun and the Earth, the particle radiation flux is significant. In this chapter, the main focus will be the radiation environment from the Sun to the upper atmosphere of the Earth. In this region of space, particle radiation can be divided into three different categories: (1) solar energetic particles, directly originating from the Sun, (2) particles trapped in the Earth's magnetic field, and (3) Galactic Cosmic Rays (GCR). These categories are discussed in the following chapter, along with the monitoring and forecasting of space weather, and its implications for our everyday life.

#### 1.1.1 The Sun

Near the Earth, the Sun is the dominant radiation source; the majority of particle radiation present in the interplanetary space near the Earth or trapped in the Earth's magnetosphere originates from the Sun. In addition to electromagnetic radiation, the solar wind mostly consists of energetic electrons and protons. In the solar wind, the plasma travels through space with an average velocity of approximately 400 km/s, and the average proton densities, in the absence of any major solar events, are in the order of  $1^{-10}$  protons/cm<sup>3</sup> [1]. This yields average proton fluxes of  $4 - 40 \cdot 10^7$  cm<sup>-2</sup>s<sup>-1</sup>.

#### 1.1.2 The Sunspot Cycle

The Sun's activity fluctuates with a period of approximately 11 years, which is called the solar cycle. The activity of the Sun is closely related to the number of sunspots observed in the Sun's surface. The first European observations of the sunspots were made in the 17th century, but the daily records were started in 1749 [2]. There are some scarce records available, dating back to the year 1610. The counting of these cycles was started in the 1760s, when the occurrence of the first official full cycle has been agreed; in 2017, the 24th cycle is ongoing. The monthly average of the sunspot number from Ref. [2]

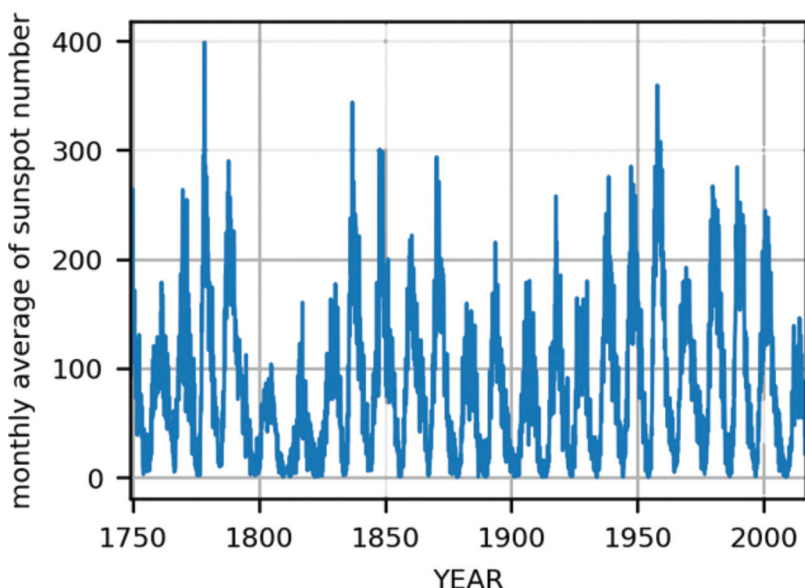


**Figure 1.1** Monthly average of sunspot number from the beginning of 1749 to September 2016 as taken from Ref. [2].

is presented in Figure 1.1. The “11-year” periodicity in the sunspot number is clearly seen in the figure.

### 1.1.3 Solar Flares and Coronal Mass Ejections

Apart from the fairly predictable solar cycle discussed above, there are also unpredictable phenomena occurring in the Sun. Sometimes, interactions between the hot plasma and the magnetic fields on the surface of the Sun lead to the expulsion of vast quantities of plasma. These eruptions are called solar flares, and the most massive solar flares are called Coronal Mass Ejections (CMEs). CMEs are orders of magnitude larger compared to regular solar flares. In CME events, a large part of the Sun’s corona is ejected from the Sun with velocities up to thousands of kilometres per second, with ejecta mass up to  $10^{13}$  kg [5].

The solar flares mainly consist of electrons and protons, but there are also heavier ions, such as oxygen and iron, present in these shockwaves. In Figure 1.2, the average particle fluxes in the solar wind for oxygen and iron ions are presented as they have been measured by the Solar Isotope Spectrometer [6] on board the Advanced Composition Explorer spacecraft [3].

## 4 Space Radiation Effects in Electronics

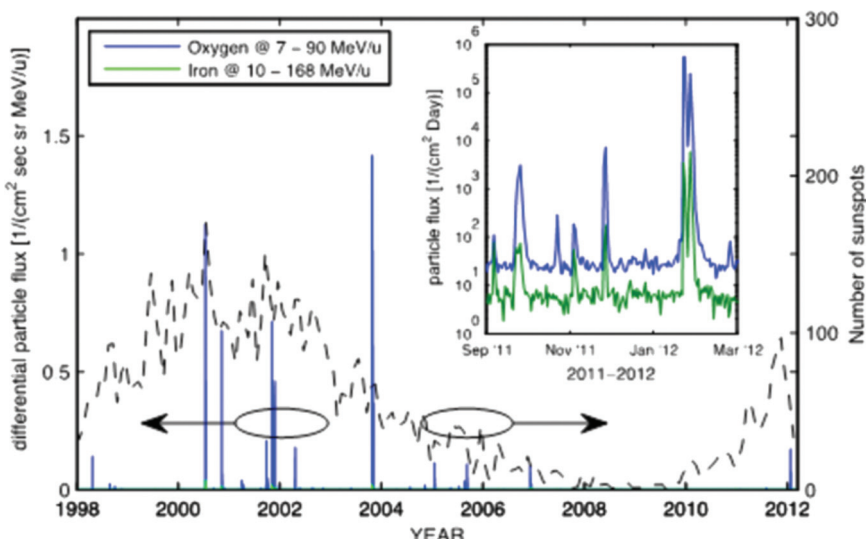


**Figure 1.2** Daily average of solar energetic particle fluxes from 1998 to March 2012 for oxygen and iron ions measured by the Solar Isotope Spectrometer on the Advanced Composition Explorer spacecraft [3], with monthly average sunspot number taken from Ref. [2]. Particle flux data are taken from Ref. [1]. Figure taken from [4].

These data are available online from Ref. [1]. The graph presents the data taken between two solar maxima around years 2001 and 2012. In the graph, the solar activity is presented by the monthly averaged sunspot number from Ref. [2]. The data clearly demonstrate the increased occurrence of bursts in the heavy-ion fluxes during the high activity season of the Sun. The variability in the ion fluxes is more easily observed in the inset graph. The observed peaks are associated with solar flares, and the highest ones are due to CMEs. Although the amount of heavier ions in CMEs is much lower than that of the solar wind protons or electrons, they can cause problems in the electronics more easily due to their higher ability to ionize matter (i.e. stopping force). More discussion on the particle–matter interactions in materials and particle-induced effects in electronics is presented below.

### 1.1.4 Trapped Particles – Van Allen Belts

The Earth's magnetic field and atmosphere prevent the energetic charged particles from directly reaching the Earth's surface. As the fast-moving charged particles enter the Earth's magnetosphere, they experience tangent Lorentz forces which bend their trajectory. This trajectory bending can lead

to particle trapping in the magnetosphere, thus creating regions with high radiation fields known as the Van Allen belts [7]. These belts mostly consist of energetic protons and electrons. There are two distinct regions called the inner and outer belts: the inner belt is generally referred to as the proton belt and the outer one as the electron belt, because these regions are dominantly populated by these particles.

### 1.1.5 South Atlantic Anomaly

The Earth's magnetic poles (North pole: 85.01°N, 132.66°W, South pole: 64.43°S, 137.32°E [8]) diverge from the geographical poles. In addition, the magnetic poles are not antipodal, in contrast to the geographical poles which are antipodal by definition [8]. This misalignment causes eccentricity in the Van Allen belts with respect to the Earth's surface. Hence, there is an increased amount of energetic particles reaching very low altitudes in the South Atlantic region east of Brazil. This region is called the South Atlantic Anomaly (SAA). The SAA is illustrated in Figure 1.3, where the fluxes

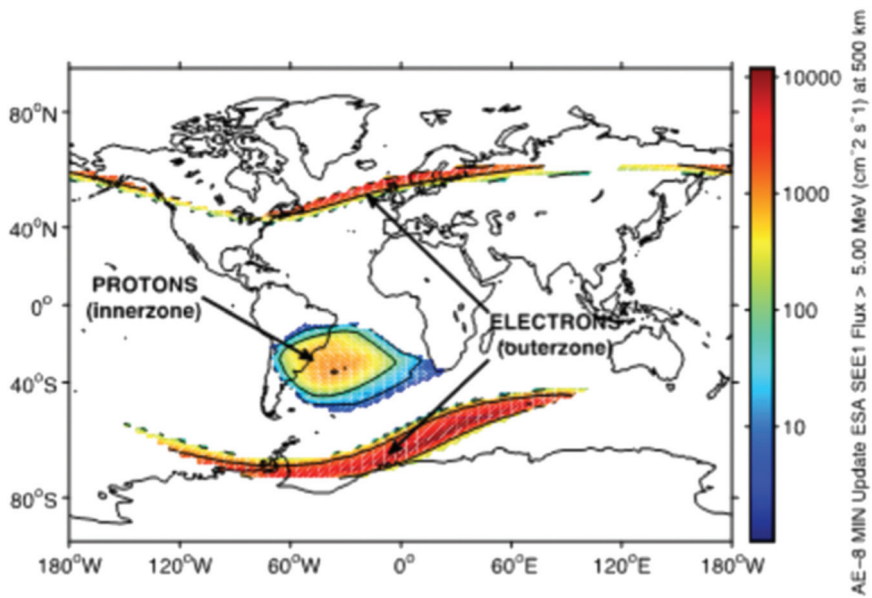


**Figure 1.3** Proton (100 MeV) and electron (5 MeV) intensities at 500 km altitude estimated by the AP8-MIN and AE8-MIN models, respectively [19, 20]. The South Atlantic Anomaly can be clearly seen in the south-east coast of Brazil, where there is a distinct region of energetic protons reaching altitudes of 500 km. Data taken from the ESA's Space Environment Information System (SPENVIS) in Ref.[9]. Figure taken from Ref. [4].

## 6 Space Radiation Effects in Electronics

of  $>100$  MeV protons and  $>5$  MeV electrons at an altitude of 500 km are presented as taken from Ref. [9]. One should note that in this figure, the SAA region consists only of protons at the given energies. The SAA exposes high-altitude aircrafts to higher radiation levels than other regions around the globe. Moreover, the SAA poses a severe threat to satellites orbiting the Earth.

### 1.1.6 Galactic Cosmic Rays

Satellites orbiting the Earth below the Van Allen belts, in Low Earth Orbit (LEO), are experiencing relatively low and stable radiation fluxes, with occasional disruptions by high solar activity (i.e. solar flares and CMEs, see discussion above) and passages through the South Atlantic Anomaly. The radiation environment within and outside the radiation belts is much more irregular and influenced by the solar activity.

Aside from the solar contribution to the radiation environment, a relatively steady flux of ions at very high energies can be identified. These particles are called Galactic Cosmic Rays (GCR), as they originate from supernovae in other galaxies. Their energies can reach up to several hundreds of GeV/u. By using the CREME code, available online at Ref. [10], the radiation environment due to GCRs can be estimated. GCR spectra at the Geostationary Earth Orbit (GEO) or in near-Earth interplanetary space are presented in Figure 1.4.

In Figure 1.4, the differential fluxes of selected GCR particles are given as a function of energy per nucleon. The fluxes are defined after 2.54 mm of aluminium, which are a typical shielding thickness and material for spacecraft. The selected particles are proton, helium, carbon, silicon and nickel. The particle fluxes are plotted according to the estimations for solar minimum and maximum. The difference in the GCR spectra, presented in Figure 1.4, between the solar maximum and minimum, is due to the variation of the intensity of the interplanetary magnetic field, which is correlated to the solar activity. High solar activity during the solar maximum gives rise to higher solar magnetic fields, and thus lower-energy GCRs are deflected away from the inner planets of the Solar System.

Among GCRs, protons are the most abundant species, as can be seen in Figure 1.4. This trend is also illustrated in Figure 1.5, where the relative abundances of particle species are presented as a function of atomic number. This graph shows the rapid drop in particles with atomic numbers above that of iron ( $Z \sim 26$ ). This is due to the maximum in the nuclear binding energy for atomic masses around  $A = 60$ . For simulation purposes, this results in a practical maximum value for the electronic stopping force in silicon of GCRs

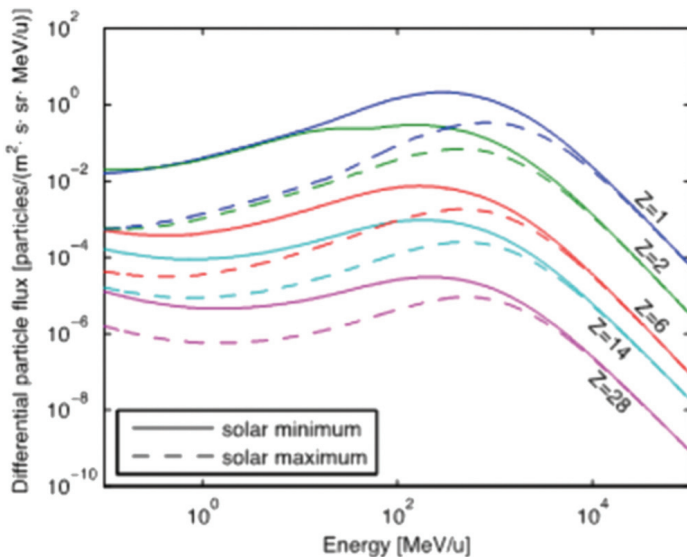


**Figure 1.4** Differential flux of selected galactic cosmic ray particles after 2.54 mm of aluminium as a function of energy per nucleon in GEO or near Earth interplanetary space during the solar minimum (solid line) and the solar maximum (dashed line). Data are taken from [10]. Figure taken from Ref. [4].

to be approximately 30 MeV/(mg/cm<sup>2</sup>). More discussion of the electronic stopping and the radiation effects and their testing in electronics are presented below.

### 1.1.7 Space Weather

The space radiation environment (also called “space weather”), is constantly monitored by various dedicated satellite systems, such as the Geostationary Operational Environmental Satellites (GOES) and the Solar and Heliospheric Observatory (SOHO). For instance, the Space Weather Prediction Center (SWPC) of the National Oceanic and Atmospheric Administration (NOAA) provides a service for real-time monitoring and forecasting of the space environment. Their webpages can be found at <http://www.swpc.noaa.gov/>. Real-time information about the space radiation environment is crucial for the safety of modern satellite systems, and also to some extent for electronic and electrical systems on the ground. While smaller solar flares are only a threat to spacecraft, the most intense flares (CMEs) can create geomagnetically induced currents (GIC) on the Earth’s surface which can also affect the power

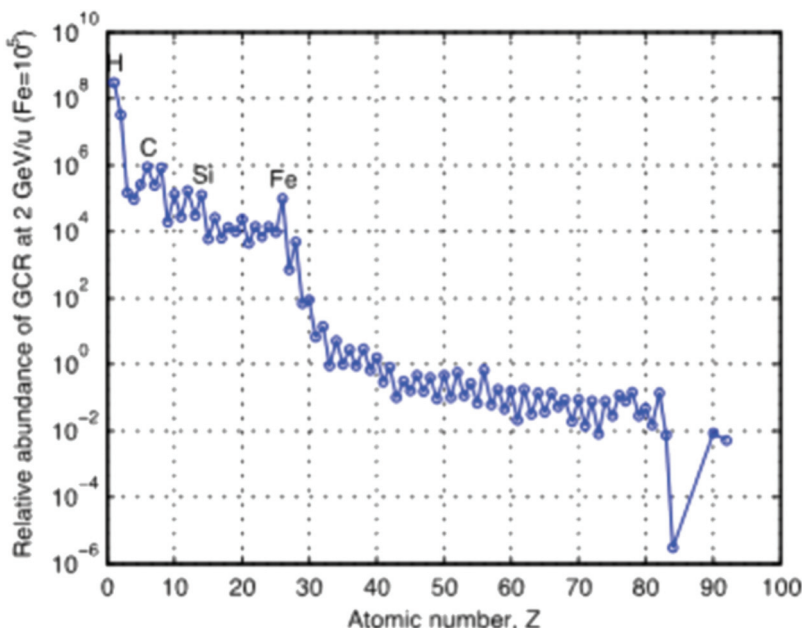


**Figure 1.5** Relative abundance of different ion species in galactic cosmic rays as a function of atomic number at energies  $\sim 2$  GeV/u. Data are taken from [10]. Figure taken from Ref. [4].

grids, telecommunication networks, pipelines and railways. The GICs and their effects in the power lines in Finland have been discussed in Ref. [11]. The solar flares also increase the radiation levels in the atmosphere due to the increase in trapped particles in the Van Allen belts. The most well-known and easily observable indication of increased atmospheric radiation are the northern and southern lights, which are also known as the Aurora Borealis and Aurora Australis. These phenomena are caused by interactions between space radiation and atmospheric gas at high altitude.

### 1.1.8 Atmospheric and Ground-Level Radiation Environments

Particle radiation is not restricted only to space. Natural and artificial sources of particle radiation may be found on Earth at high altitude, on the ground and underground, and have been shown to affect electronics. This section gives a brief introduction to the radiation sources existing at the ground level and in the Earth's atmosphere. First, we present a discussion on the natural sources, followed by a short contemplation of the artificial sources.

### 1.1.9 Cosmic Rays

Although the Earth's magnetic field deflects the majority of the particle radiation coming from space, there is still a continuous shower of energetic particles present at high altitudes and even at the ground level due to the GCRs and the solar activity. The atmospheric radiation was shown to increase with altitude already 100 years ago by Victor Hess, who also proved the radiation to be mostly of cosmic origin [12].

The probabilities of the primary cosmic ray particles (protons and heavy ions) themselves penetrating the atmosphere are extremely low, but as they interact with atoms in the upper atmosphere, secondary energetic particles are released, such as neutrons and muons. These secondaries interact relatively weakly with matter, and they are able to reach ground level, and to some extent even penetrate the Earth. Neutrons, being neutral particles, do not interact with matter via Coulomb forces and thus no primary ionization is produced by them. In turn, neutrons can indirectly produce ionizing effects via scattering with nuclei, elastically or inelastically.

Early in 1979, Ziegler and Lanford in Ref. [13] suggested that the anomalous soft errors observed in random-access-memories (RAM) were caused by atmospheric neutrons. They also predicted this effect, at that time considered quite minute, to become more pronounced in the future along with the technological evolution. In his review in Ref. [14], Normand discussed the impact of the two papers, Refs. [13], [15], on the activities of the electronics industry. Normand criticized that the susceptibility of electronics to errors induced by atmospheric neutrons remained publicly unrecognized. Even though the vendors (e.g. IBM [16]) made extensive studies about the subject early on, they published the results much later. Normand's paper presents several examples of soft error observations in memories and explains them with the atmospheric neutrons. The impact of atmospheric neutrons on scaled technologies has been discussed recently by Ibe et al. in Ref. [17], where, based on their simulations, they confirm Ziegler's postulate that the effect becomes more pronounced along with the technology scaling. Some anecdotal suggestions have been made by representatives from electronics industry about the increasing possibility of cosmic rays causing failures in the evolving automotive electronics if not taken into account in the design [18]. This aspect is also discussed in Ref. [19 and references therein].

Atmospheric radiation is more of a problem in avionics. After the solar flare occurred in late January 2012 (see the inset of Figure 1.2), several airlines were forced to divert their flights from the polar routes due to increased

radiation in the atmosphere [20]. The effects of cosmic rays on avionics has been discussed, e.g. in Refs. [21, 22].

Apart from neutrinos, muons are the most abundant of the cosmic ray secondaries present on the ground [23]. Muons are a charged particle with the same charge as electron, and mass corresponding approximately 200 times the electron mass. The first results on muon-induced errors in microelectronics were published by Sierawski et al. [24], where an artificially produced muon beam was used. Additional results from irradiations of SRAM memory components with low-energy muon beams were reported in [25, 26]. These results suggest that while low-energy muons are capable of inducing single-event upsets in 65 nm and smaller technology nodes in a lab environment, atmospheric muons (which have relatively high energy and low electronic stopping force) are incapable of doing so. However, these results predict the susceptibility of components to become higher in the future technologies.

### 1.1.10 Radionuclides in the Soil

Although silicon is the second most abundant element (by weight) in the Earth's crust [27], the use of this excellent metalloid in semiconductor industry has exhibited some unexpected problems in the past. Trace radioactive elements are present everywhere in the soil; thus, all bulk materials contain small traces of radioactive particles, even after refinement. The most concern is due to U-238 and Th-232, and their radioactive daughter nuclides, such as Rn-220 and Rn-222.

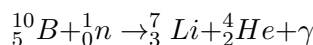
In 1979, May and Woods reported in Ref. [15] that alpha particles emitted from the packaging materials were causing soft errors in random access memories (RAM) and charge-coupled-devices (CCD). It was shown that the packages used at that time contained these radioactive elements in the order of some parts per million. In 1982, the metal layers within integrated circuits was demonstrated to be another possible source of radioactivity [28]. After these revelations, efforts were made to eliminate these sources of radiation and mitigate their effects, typically by enhancing the purity of the materials and/or implementing error detection and correction (EDAC) in these devices. In addition, protective coatings on the device surface have been introduced in order to minimize the problem [29]. However, these "auxiliary" materials are not the only source of radiation. Even after silicon goes through a thorough refining process, trace amounts (~parts per billion) of these unwanted radioactive elements remain present, which in turn have been demonstrated to cause soft errors in modern memories [30, and references therein].

Radon is a radioactive gas which is naturally found around certain types of soil, and is a well-known health hazard. A recent study presented in Ref. [31] has shown that ambient radon is very unlikely to induce errors in microelectronics via diffusion through the packaging. Nevertheless, while being an inert atom, Rn can diffuse into materials. Also, its daughter nuclides, usually positively charged ions, can adhere to surfaces [32]. These radioactive elements have to be taken into account in devices with bare dies such as particle detectors.

These problems, caused by the radioactive residues, are nearly impossible to avoid completely. Only very strict control of the materials used in manufacturing and robust EDAC techniques are effective in assuring the tolerance to these radiation sources.

### 1.1.11 Thermal Neutrons

Eventually, if they are not captured by target material, the secondary neutrons (produced by either the aforementioned cosmic rays, or decay of radionuclides in the soil) lose most of their energy and become thermalized. These so-called thermal neutrons have an average kinetic energy of  $\sim 25$  meV, which is the most probable energy for a free particle at room temperature ( $\sim 290$  K). It was discovered by Fermi et al. (see Ref. [33, and references therein]) that slow neutrons are more effectively interacting with matter than high-energy ones. Thermal neutrons can initiate nuclear reactions, if they are captured by target nuclei. Depending on the target atom, the reaction products can be either gamma rays or particle radiation. If particle radiation is released in the reaction (especially for fission products), a large amount of ionization will be generated around the site of the interaction, which can be a source of errors in electronic components. The most notorious example of this phenomenon is the thermal neutron-induced fission of boron-10 described by



This is due to  ${}_{5}^{10}B$  having an exceptionally high cross-section for thermal neutron capture, when compared with other materials. This has been shown, in Ref. [34], to be a considerable source of errors in Static Random Access Memories (SRAM). Due to the relatively high fluxes of low-energy neutrons and their high penetration capability, the only way to mitigate this problem is to avoid using  ${}_{5}^{10}B$  in the devices. Boron is a very widely used dopant in semiconductors, and is present in the borophosphosilicate glass (BPSG) commonly used as an insulator in standard manufacturing processes. Although

## 12 Space Radiation Effects in Electronics

naturally  $^{11}_5B$  is the most abundant ( $\sim 80\%$ ) boron isotope, the boron used in manufacturing has to be carefully refined to eliminate the  $^{10}_5B$ , in order to minimize the problems caused by thermal neutrons.

### 1.1.12 Artificial Radiation Sources

In addition to natural sources, there are a lot of man-made radiation sources at ground level; radiation from these sources can be a reliability issue for electronic systems. A selected list of man-made radiation sources is given below.

- accelerators, e.g. cyclotrons (heavy ions, protons, neutrons, electrons), synchrotrons (X-rays) and X-ray tubes;
- lasers;
- radionuclides (photons, electrons, neutrons, protons, heavy ions);
- nuclear power plant (photons, neutrons);
- nuclear weapons (e.g. Operation Dominic [35, 36]).

Extra care has to be taken of electronic systems used in the vicinity of these artificial radiation sources, in order to assure their operation. For example, in nuclear power plants or accelerators, such as the Large Hadron Collider at CERN, electronics failures must be minimized to ensure the reliable and safe operation of the whole facility. The radiation sensitivity of exposed electronics must be tested, and in some situations, equipment must be implemented using radiation-hard parts (RadHard). The use of accelerators, namely cyclotrons, and enriched radionuclides, in the radiation effects testing of electronics is discussed later in this book.

## 1.2 Radiation Effect in Materials and Devices

### 1.2.1 Energetic Charged Particles and Matter

While an energetic charged particle traverses matter, it loses energy via different mechanisms. A simple illustration of energy loss is given in Figure 1.6, where an ion with initial energy of  $E$  penetrates a slab of material with a thickness of  $\Delta x$ . The final energy of the ion is  $E - \Delta E$ . If the thickness is considered as infinitesimal,  $dx$ , the energy loss  $\Delta E \rightarrow dE$ . From this, the total stopping force is defined as

$$-\frac{dE}{dx} \Big|_{total} = \sum_i -\frac{dE}{dx},$$

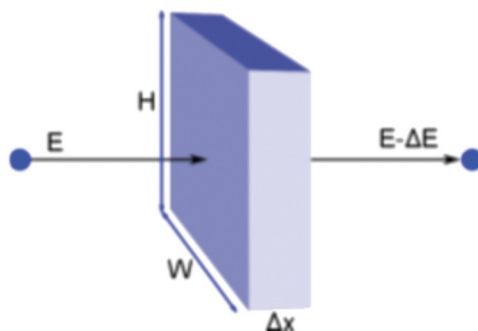


**Figure 1.6** Illustration of the energy loss of energetic particle with initial energy of  $E$  after passing through a slab of material with thickness of  $\Delta x$ .

where  $i$  denotes the different energy loss mechanisms according to [37], which are listed below:

1. Excitation and ionization of target atoms;
2. Projectile excitation and ionization;
3. Electron capture;
4. Recoil loss (“nuclear stopping”) and
5. Electromagnetic radiation.

Additionally, part of the energy loss can also go to the following reactions:

6. Nuclear reactions and
7. Chemical reactions

As in this work, primarily the interactions between heavy ions and matter are considered at energies of hundreds of keV/u to tens of MeV/u, mechanisms 1–4 are the most relevant ones. Moreover, this chapter concentrates on mechanisms 1 and 2 as they constitute most of the electronic energy loss, which dominate above all others in the energy ranges and ion species studied in this work. Nuclear reactions (6) are discussed, as there is evidence of their contribution in the errors observed in modern electronics. Nuclear stopping (4) is also briefly discussed.

Particle radiation can change the physical properties of the target material, both temporarily and permanently. Usually, ionizing radiation (processes 1–3) is considered to be non-destructive, as it is mainly breaking the covalent bonds in the target material. Depending on the material, these broken bonds may be self-reassembled immediately after their creation, or can be repaired by high-temperature annealing. In reality, heavy ions also

create permanent changes in the target. This is, on the one hand, due to the high density of ionization caused by the high-Z ions, which induces material modification. On the other hand, energetic target recoils, due to nuclear stopping (4), may modify the atomic structure of the target. In some cases, depending on their nature, these atomic defects can also be repaired by high-temperature annealing. The effects of energetic heavy ions in materials and electronic devices are discussed below.

### 1.2.2 Stopping Nomenclature

Before proceeding, the terminology of the energy loss will be clarified. Typically, the energy loss of an ion in matter is called the stopping power. In the past, there has been intensive discussions on the terminology, whether the term “stopping power” should be replaced by stopping force [38]. In this text, the term “stopping force”, or simply “stopping”, is used.

### 1.2.3 General Theory for Electronic Stopping

When considering the mean energy loss per unit length for a projectile due to the collisions with target electrons (i.e. electronic stopping force), it is generally written as:

$$-\frac{dE}{dx} \Big|_{elec} = NZ_2S = \frac{1}{4\pi\epsilon_0^2} \frac{Z_1^2 q^4}{m_e v^2} NZ_2 L = 3.0705 \cdot 10^{-4} \frac{Z_1^2 Z_2}{A_2 \beta^2} L, \quad (1.1)$$

where

$Z_{1,2}$  are the atomic numbers for the projectile (1) and target (2);

$A_2$  is the mass number of the target atom;

$N$  is the atomic density of the target material;

$v$  is the velocity of the projectile;

$S$  is the electronic stopping cross section in units of [*energy* × *area*];

$q$  and  $m_e$  are the elementary charge and the electron rest mass, respectively;

$\epsilon_0$  is the vacuum permittivity and

$L$  is the theory dependent dimensionless stopping number (see below).

Furthermore,  $\beta = v/c$  and  $c$  is the speed of light in vacuum. The electronic stopping force in Equation (1) is given in units of MeV/(mg/cm<sup>2</sup>).

The sophisticated reader might notice that this is the unit for mass stopping force and not for stopping force (MeV/ $\mu\text{m}$ ). Let us clarify here that in this work, the concepts of mass stopping force and stopping force are used interchangeably, although technically there is a difference. Strictly speaking, the mass stopping force is the stopping force divided by the density of the target material (i.e.  $-\frac{1}{\rho} \frac{dE}{dl}$ ).

In the following sections, the fundamental stopping theories by Bohr, Bethe and Bloch are introduced. Also, description of a semi-empirical model developed in this work is given below.

#### 1.2.4 Stopping Theories and Semi-Empirical Models

Probably, the most widely known and used notation for the electronic stopping force is the Bethe formula, where the stopping number is

$$L_{Bethe} = \ln \frac{2m_e v^2}{\hbar \omega_0} \quad (1.2)$$

This equation is based on the quantum mechanical treatment of the interaction between the projectile and the target electrons. It should be noted that this equation is valid when  $2m_e v^2 \gg \hbar \omega_0$ . A comprehensive derivation of Equation (2) is presented in Refs. [37, 39].

Another well-known notation for electronic stopping force is from the Bohr's classical theory. Niels Bohr formulated his theory on the decrease of velocity of moving electrified particles on passing through matter in 1913 [40], which he later revised in Refs. [41, 42]. The Bohr's model is approximately valid for velocities

$$\beta < 2Z_1\alpha, \quad (1.3)$$

where  $\alpha \sim \frac{1}{137}$  is the fine structure constant. The lower limit of validity is set by  $\beta \gg \alpha$ . In the classical picture, the target electrons are treated as harmonic oscillators with resonance frequencies of  $\omega_i$ . The collisions are considered as elastic. From this treatment on the interaction between the impinging energetic ion and an individual target electron, Bohr's stopping number becomes

$$L_{Bohr}(\xi_i) = \ln(C\xi_i), \quad (1.4)$$

where  $\xi_i = \frac{m_e v^3}{Z_1 \cdot \alpha \cdot c \cdot \hbar \cdot \omega_i}$  and  $C = 2e^{-\gamma} \cong 1.1229$ . Here,  $\gamma$  is the Euler-Mascheroni constant usually known as the Euler's constant (not to be

confused with the Euler's number  $e = 2.71828\dots$ ). By summing over all electrons in the target atom, we get

$$L_{Bohr} = \sum_i f_i \ln(C\xi_i) = \ln(C\xi), \quad (1.5)$$

where  $f_i$  is the weighting factor corresponding to the individual electron ( $\sum_{i=1}^{Z_2} f_i = 1$ ). Now, we can write

$$\xi = \frac{m_e v^3}{Z_1 I \alpha c}, \quad (1.6)$$

where  $I = \hbar\omega_0$  is the material-dependent mean excitation energy corresponding to the mean frequency.

At low projectile velocities, there is a drawback in Equation (5), i.e.  $\xi \leq \frac{1}{C} \Rightarrow L_{Bohr} \leq 0$ . Solution to this problem has been presented in Ref. [37], where the works of Lindhard and Sorensen [43] are articulated. In this derivation, the Bohr's stopping number becomes

$$L_{Bohr} = \frac{1}{2} \ln[1 + (C\xi)^2]. \quad (1.7)$$

There is a myriad of semi-empirical approaches for estimating the electronic stopping force.

### 1.2.5 Nuclear Stopping Force

The nuclear stopping is the part of the projectile's energy loss due to Coulombic interaction between the target and the projectile nuclei. With a similar treatment as for the electronic stopping above, a general equation for nuclear stopping force can be written as

$$-\frac{dE}{dx} \Big|_{nucl} = \frac{1}{4\pi\epsilon_0^2} \frac{Z_1^2 Z_2^2 q^4}{M_2 v^2} N L_{nucl}, \quad (1.8)$$

where the notations are the same as in Equation (1) and, in addition,  $M_2$  is the mass of the target nucleus. The nuclear stopping relative to electronic stopping can be estimated by dividing Equation (8) with Equation (1) yielding a ratio of

$$\frac{-\frac{dE}{dx}|_{nucl}}{-\frac{dE}{dx}|_{elec}} = \frac{m_e}{M_2} Z_2 \frac{L_{nucl}}{L_{elec}} \approx 2.7 \cdot 10^{-4} \frac{L_{nucl}}{L_{elec}}. \quad (1.9)$$

From this, it can be seen that the contribution of the nuclear stopping in the total stopping force is several orders of magnitude lower than that of the electronic stopping. This holds at projectile velocities typically used in radiation effects testing discussed later in the text. The ratio of the stopping numbers, and thus the nuclear stopping, becomes significant only at low ion velocities [37]. Even though in the nuclear stopping process the energy lost by the projectile is transferred mainly to the kinetic energy of the target nucleus, and the recoil loses its energy partly via electronic stopping, the ionization effect is typically considered to be less significant. The effect of nuclear stopping is typically attributed to the displacement damage (DD) effect, discussed later in the text.

### 1.2.6 Ion-induced Nuclear Reactions

As mentioned above, ions can lose their energy also by inducing nuclear reactions. The cross sections for the nuclear reactions are much lower than the ones for the other mechanisms discussed above, and they are typically neglected. This is especially the case for heavy ions. Nevertheless, in microelectronics, the products from the nuclear reactions may induce failures. Thus, the ion-induced nuclear reactions are briefly introduced here.

When considering positively charged projectile ( $Z_1, A_1, R_1$ ) and target ( $Z_2, A_2, R_2$ ) nuclei, there is a repulsive electromagnetic force acting on them. Here,  $Z_i, A_i$  and  $R_i$  correspond to the atomic and mass numbers and the radii of the nuclei, respectively. The radius of a nucleus is typically estimated

$$R_i = R_0 \cdot A_i^{1/3} fm, \quad (1.10)$$

where  $R_0$  is an empirical constant. Typically,  $R_0 = 1.2 fm$  is used. This constant can vary in the range of  $1 fm < R_0 < 4.5 fm$ , depending on the nucleus [44].

In order for a nuclear reaction to occur, the nuclei need to be in close contact. This means that the impact parameter has to be less than the sum of the radii of the nuclei,  $R = R_1 + R_2$ , and the total kinetic energy in the system has to exceed the potential energy formed by the repulsive Coulombic force. This limit in the potential energy is called the Coulomb barrier, which can be estimated by

$$U_{CB} = \frac{1}{4\pi\epsilon_0} \frac{Z_1 Z_2 e^2}{R} \approx 1.2 \frac{Z_1 Z_2}{A_1^{1/3} + A_2^{1/3}} MeV. \quad (1.11)$$

From the conservation laws of momentum and energy, the threshold kinetic energy in the laboratory frame for the projectile to overcome the Coulomb barrier can be written as [44]

$$K_{cbt} = U_{CB} \cdot \left(1 + \frac{A_1}{A_2}\right). \quad (1.12)$$

For light projectiles, where  $A_1 \ll A_2$ , the kinetic energy threshold is essentially the same as the Coulomb barrier given by Equation (11). Classical estimation for the maximum total cross section for nuclear reactions is given by

$$\sigma = \pi R^2 \cdot \left(1 - \frac{K_{cbt}}{E_k}\right), \quad (1.13)$$

where  $E_k$  is the initial kinetic energy of the projectile [45].

## 1.3 Radiation Effects in Semiconductors

This chapter presents different phenomena occurring in materials due to the energy deposition by these particles. From electronics' point of view, the most relevant materials are silicon (Si) and silicon dioxide ( $\text{SiO}_2$ ). In some examples in the text, also other materials may be mentioned.

Typically, in electronics, the generation of electron–hole pairs (e–h) due to the energy deposition of any quantum of ionizing radiation (photon or particle) is considered to be the dominant effect. The atomic displacements are considered to play a minor, but still in some cases, a relevant role. This will be discussed below.

When considering the influence of particle radiation in electronics, typically only the electronic stopping force is considered. The electronic stopping force can be related directly to ionization, whereas nuclear stopping and other mechanisms are only causing ionization indirectly. Nuclear reaction products and elastic recoils can also cause ionization, but usually in case of heavy ions, their contributions are neglected. However, recently, there has been an increasing interest toward their contribution, as discussed in Ref. [14, and references within]. The effects of nuclear reactions in materials and devices are briefly discussed below.

### 1.3.1 Generation of Electron–Hole Pairs

At room temperatures, the energy gap in the silicon band structure is 1.1 eV [47] and for  $\text{SiO}_2$ , the corresponding value is 9 eV [48]. These are the

minimum energies at which the upmost electrons in the valence band (VB) are excited to the conduction band (CB). The average energies required to generate an e–h pair in Si and  $\text{SiO}_2$  are 3.6 eV [49] and  $17 \pm 1$  eV [50], respectively. This is called the mean e–h pair creation energy. When considering electronics and the e–h pairs, induced by radiation, there are three main criteria that need to be fulfilled in order to cause major ionizing radiation effects. These criteria are as follows:

The deposited energy in a single encounter between atomic electron and radiation quantum (i.e. ion, delta-electron or photon) has to exceed the band gap energy to produce an e–h pair. In practice, the number of generated e–h pairs is estimated by dividing the mean energy deposition with the mean e–h pair creation energy.

The density of induced e–h pairs has to exceed the intrinsic free electron density of the target material. Hence, in metals, the effect of ionization is negligible due to the intrinsically high count of free electrons.

An electric field is required in order to collect the excess charge carriers.

### 1.3.2 Nuclear Reactions

Even if the impinging ion itself is incapable of generating enough e–h pairs via electronic stopping mechanisms to cause disturbance in electronics, it still may induce nuclear reactions as discussed above. In turn, the reaction products may be capable of producing high-density plasma of e–h pairs. This is typically encountered with high-energy protons that exhibit low electronic stopping, but still are capable of inducing errors in the devices. These errors originate from the  $\text{natSi(p,X)Y}$  nuclear reactions, already mentioned above. An example of this phenomenon is presented in Figure 1.7, where a Single Event Upset (SEU) cross-section curve from Ref. [51] for a 4 Mbit SRAM is plotted as a function of proton energy. In this figure, it is seen that low-energy protons ( $< 20$  MeV) are less capable of producing errors in the device than high-energy protons, for which the cross section (i.e. probability) is saturated. The low-energy behaviour is due to the Coulomb barrier, discussed above, which can be estimated to be 4.3 MeV for protons in silicon. This is roughly observed in Figure 1.7, although the data are not precise enough to make solid conclusions. The saturation in the cross section originates from the limitation in the electronic stopping force for the reaction products. For example, if we consider the above-mentioned reaction, the reaction product that has the highest capability for energy deposition is phosphorus ( $Z_1 = 15$ ). The maximum energy loss value, according to SRIM, for this ion is  $15 \text{ MeV}/(\text{mg/cm}^2)$  that

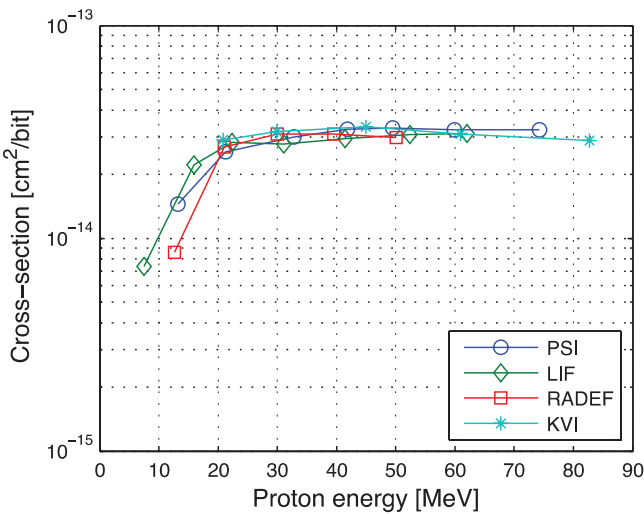


**Figure 1.7** Cross section for proton-induced SEUs as a function of proton energy measured from 4 Mbit Atmel AT60142F SRAM used in the SEU monitor [52]. Data taken from Ref. [51].

sets the upper limit for the deposited energy from the reaction. In reality, the probability for  $\text{natSi}(p,\gamma)$  P-reaction can be assumed to be lower than that for other reaction channels, but it enables the highest energy deposition.

Another demonstration of the contribution of the nuclear reactions in the energy deposition of protons in silicon is presented in Figure 1.8. In this figure, the energy deposition of 30 MeV protons in silicon target is presented as simulated with the MRED code [10]. The target was a slab of silicon with arbitrarily chosen dimensions of  $100 \times 100 \times 20 \mu\text{m}$  ( $W \times H \times \Delta x$ , see Figure 1.6). The MRED code enables the omission of the physics definitions for the nuclear reactions from the simulations. Thus, the effect of nuclear reactions is possible to indicate. The spectrum for energy deposition in Figure 1.8, with only the Coulombic scattering taken into account, exhibits a peak near 60 keV (i.e.  $3 \text{ keV}/\mu\text{m}$ ). This is comparable to the SRIM estimation for the electronic stopping force of silicon for 30 MeV protons, that is,  $\sim 3.4 \text{ keV}/\mu\text{m}$ . The spread in the spectrum is due to the straggling. The simulation, where also the nuclear reactions are included in the simulations, results in a spectrum with the same primary ionization peak, but in addition, there is a tail reaching up to 10 MeV ( $0.5 \text{ MeV}/\mu\text{m}$ ) of energy deposition within the volume. Although the probability of these events is orders of

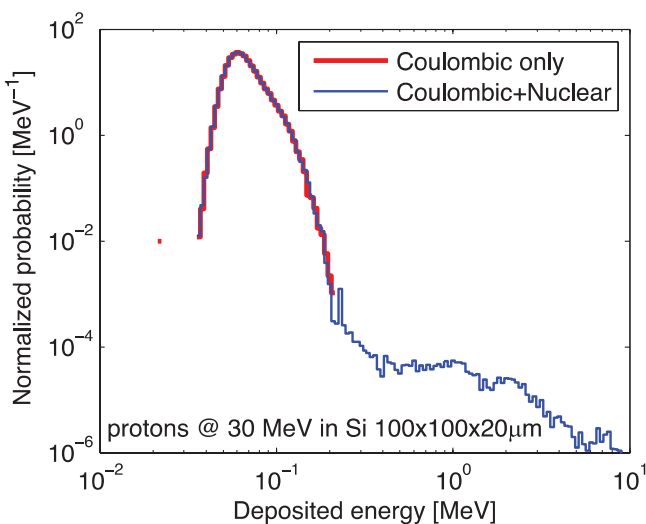


**Figure 1.8** MRED simulation of energy deposition by 30 MeV protons in silicon target with size of  $100 \times 100 \times 20 \mu\text{m}$  ( $W \times H \times \Delta x$ ).

magnitude lower than of the primary ionization, in some cases, they may turn out to be detrimental.

### 1.3.3 Linear Energy Transfer vs. Electronic Stopping Force

When discussing the ion–matter interactions, historically in medical applications and also in radiation testing of microelectronics, the term Linear Energy Transfer (LET) has been used for the average deposited energy by the impinging particle per unit length. Typically, the concepts of LET and electronic stopping force have been used interchangeably. The units of these two are the same, typically given in  $\text{MeV}/(\text{mg}/\text{cm}^2)$ . However, there is a slight difference between these two, as the electronic stopping force quantifies the mean energy lost by the particle per unit length (in collisions with the target electrons). In case of bulky objects, e.g. old technology electronic components with large sensitive volumes (SV), where the energy is deposited, this is a valid choice. Historically, in radiology, the irradiated tumours have been considered to be bulky, thus justifying the use of mean energy loss as a metric for the mean energy deposition. For a long time, in both communities, considering either radiation effects in the electronics [53–56] or the radiology [57–60], there has been discussions about the validity of LET as a metric and the comparability of LET and electronic stopping force. Although in biology

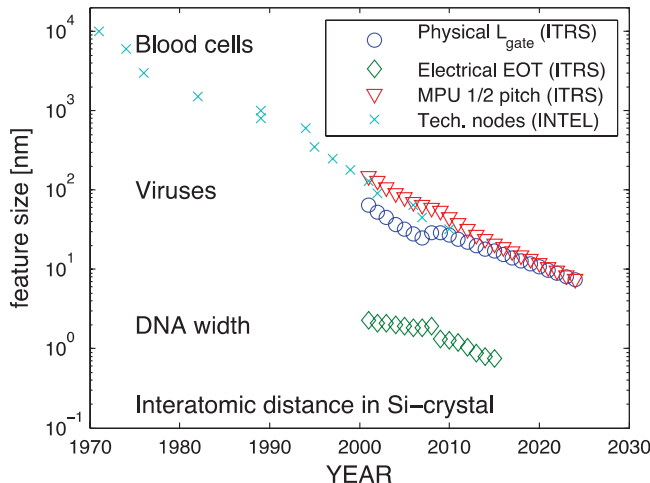


**Figure 1.9** Scaling trends of some feature sizes in microelectronics, including physical gate length ( $L_{\text{gate}}$ ), electrically equivalent oxide thickness (EOT) and half-pitch in MPU presented by the ITRS [62] and development of Intel's® technology nodes [63]. Also approximates of biological and physical feature sizes are illustrated. Figure taken from Ref. [4].

the radiation effects are shown [61] to be rather complicated, the similarity in these two different fields is in the feature sizes, where the radiation effects take place. In radiology, the noteworthy effects are considered to occur in very small dimensions, e.g. width of a DNA double strain, which have become comparable to the evolved feature sizes in modern microelectronics. In Figure 1.9, the scaling trends of some key feature sizes in electronics set by the International Technology Roadmap for Semiconductors (ITRS)[62] and the Intel® corporation [63] are presented along with some typical feature sizes in nature for comparison. The applicability of LET in radiology is out of the scope of this work. In the following section, the dependence of feature size and projectile energy on the mean energy deposition, in electronics point of view, is discussed.

### 1.3.4 Spatially Restricted LET

The energy lost by an ion, discussed above, is transferred to kinetic ( $T_{\text{kin}}$ ) and potential ( $T_{\text{pot}}$ ) energy of the target electrons. In order to contemplate the spatial distribution of the deposited energy, first, the energy transfer to the target electrons needs to be defined. By rewriting Equation (2.7), the differential cross section for Coulomb scattering becomes

### 1.3.5 Energy Loss Straggling

Energy loss of an ion in a single collision with the target electron is a stochastic event considered to follow the Poisson statistics. The expressions for the stopping force, discussed above, give only the average energy loss per unit length. In relatively large volumes, this applies, but when the volume decreases, also the randomness in the energy loss, or deposition, becomes significant, in addition to the spatially restricted LET discussed above.

A simple demonstration of the dependence of the SV size on the fluctuation in the deposited energy is presented in Figure 1.11. Here, results from Geant4-simulations [92, 93] for energy deposition of 1-MeV  $\alpha$ -particles passing through silicon targets with different thicknesses are presented. The simulations were made by “bombarding” slabs of silicon (cf. Figure 1.6) with  $\alpha$ -particles. The lateral dimensions ( $W$  and  $H$ ) in the slabs were much larger than the thickness ( $\Delta x$ ). Thus, from Equation (39), the mean chord length becomes  $l = 2\Delta x$ . The effect of the spatially restricted energy deposition is considered to be less significant in this case. It is seen in Figure 1.10 that, for 1 MeV  $\alpha$ -particles, from the total energy loss  $\sim 90\%$  is deposited within 20 nm from the ion’s trajectory. Thus, we can assume in an SV with the mean

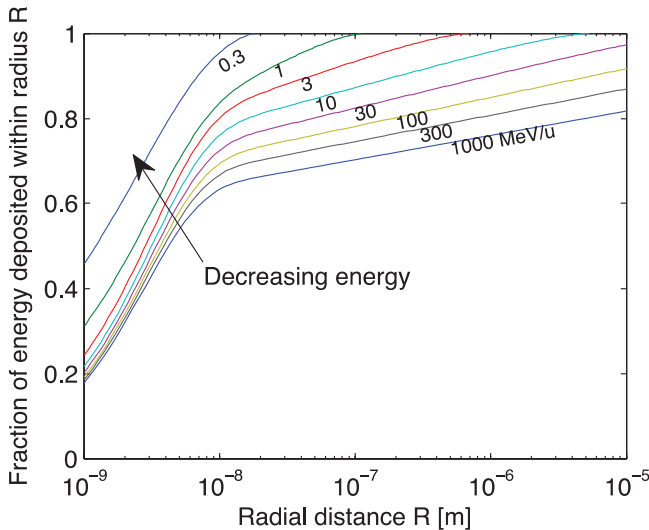


**Figure 1.10** Fraction of deposited energy within radius from the ion track as a function of radial distance for ion velocities (or energies) 0.3, 1, 3, 10, 30, 100, 300 and 1000 MeV/u, from top to bottom, respectively. Figure taken from Ref. [4].

chord length of  $>20$  nm (corresponding to the 10 nm slab), the deposited energy is more than this percentage of the average energy loss.

The shift in the spectra in Figure 1.11 to higher energies for thicker targets originates from the decrease in the ion energy (thus increase in the stopping force) along the ion's path. This increases the total deposited energy in the thicker targets compared to the average energy loss for 1-MeV  $\alpha$ -particles given by the SRIM-calculations,  $\sim 305$  keV/ $\mu\text{m}$ . Also, one should bear in mind that the descriptions for stopping in the SRIM and the Geant4 are slightly different, thus possibly yielding different average energy loss values. The physical descriptions for the nuclear reactions, discussed above, were omitted in these simulations.

The most distinct feature in this graph is the broadening of the spectra due to the straggling. The dependence of the target thickness on the broadening is clearly observed. In thin targets, the relative fluctuation in the deposited energy around the average value increases with decreasing thickness. For example, in Figure 1.11, for the 10 nm silicon target, some of the  $\alpha$ -particles deposit even twice the average energy.

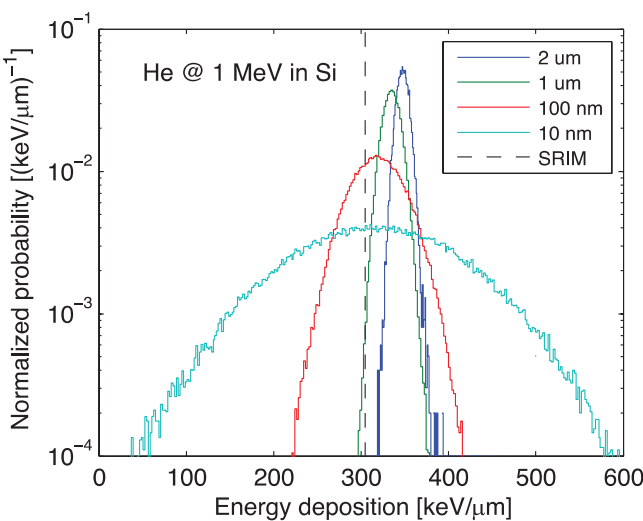


**Figure 1.11** The spectra of deposited energy from Geant4-simulations for 1 MeV  $\alpha$ -particles traversing silicon targets with thicknesses of 1  $\mu\text{m}$ , 2  $\mu\text{m}$ , 100 nm and 10 nm. The electronic stopping force value for 1 MeV  $\alpha$ -particles, taken from SRIM, is plotted with dashed line, is  $\sim 305$  keV/ $\mu\text{m}$ . Figure taken from Ref. [4].

### 1.3.6 Applicability of LET

By combining the above-mentioned aspects with the concept of LET, different regions governed by these mechanisms can be separated in the phase space determined by the ion's velocity and SV's mean chord length. These regions are depicted in Figure 1.12, where the same definitions are used as in Refs. [53, 55]. The limits drawn in the graph represent the so-called 10% thresholds, where the individual effects (spatial restriction and/or straggling) are causing more than 10% variation in the energy deposition defined by the electronic stopping. Here, the limits are calculated for protons,  $\alpha$ -particles and N-ions to demonstrate the dependence of the ion specie on the effects. The different regions in the graph are explained in the following list.

For protons and heavier ions, the LET can be considered to describe the energy deposition with sufficient accuracy.

The effect of straggling contributes to the energy deposition for protons, but for heavier ions, the use of LET is still valid.

The straggling for the  $\alpha$ -particles becomes significant.

The spatial restriction for the energy deposition comes into play for all ions, and the straggling for N-ions still plays a minor role.

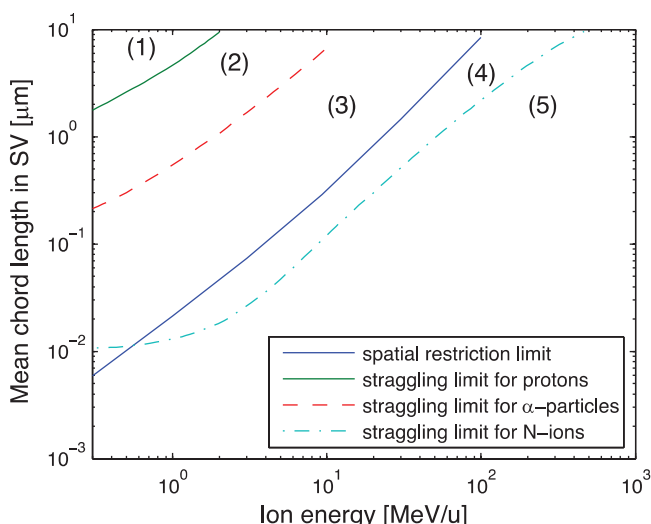


**Figure 1.12** Regions of mean chord length and ion energy (MeV/u) where parameters LET, straggling and spatial restriction affect the energy deposition. The different regions (1)–(5) are explained in the text. Figure taken from Ref. [4].

For N-ions, all three concepts, the LET, its spatial restriction and the straggling, need to be taken into account when considering the energy deposition.

The above discussion shows that when the technology is approaching the nanoscale, the conventional description of LET becomes increasingly insufficient to characterize the phenomena in the electronics. Thus, more sophisticated models would be needed. At this point, there is no simple concept to replace the LET as a metric used in the field of radiation effects in electronics.

### **1.3.7 Prediction Tools for Stopping Force**

Because no consensus has been reached on the alternatives among the community, the LET concept has yet remained in use in the characterization of the radiation effects. Moreover, as the concepts of the spatially restricted LET and the straggling require information on the SV(s) in the studied structures, which is usually unavailable, the values of electronic stopping force are used as the LET. For estimating the electronic (and in some cases also nuclear) stopping for a given ion in a given target, there is a variety of tools available, both semi-empirical and theoretical, in addition to tabulations of experimental data. A collection of LET prediction tools and data tables are presented in Table 1.1 with a brief introduction. From the listed tools, the SRIM code has received the widest acceptance among the users, and at least in the radiation effects community, it is the primary repository of stopping force values. This is due to its user-friendly interface, and in average, if all ion-target combinations are accounted for, its accuracy is fairly good.

In addition to these tools listed in Table 1.1, the Geant4 simulation toolkit [74] has become increasingly into use in predicting radiation effects in electronics. The disadvantage in the Geant4 calculations is the relatively high threshold for deployment. On the other hand, the Geant4 is a powerful tool to investigate radiation effects in complex volumes. There is also a Geant4-based Monte-Carlo Radiative Energy Deposition (MRED) tool developed in Vanderbilt University, USA, which is available online [10]. This tool enables estimations for the particle-induced energy deposition in complex geometries via a user-friendly interface. For this tool, user registration is required, whereas the Geant4 is fully open source.

All the above mentioned are estimation tools (except the data tables), and they provide estimations for the stopping force. Each of them have

**Table 1.1** Stopping force prediction tools.

Source	Type	Description
SRIM [64]	Semi-empirical	The most well-known of them all. Based on the work of Ziegler et al. described in Ref. [94]. Over the years, numerous updates have been made in the calculations. Last major update was in 2003. This code and its user interface are very versatile and user-friendly. It enables calculations for a wide energy range with huge variety of ion-target combinations with a reasonable accuracy. Software is freely available at <a href="http://www.srim.org">http://www.srim.org</a> .
LET Calculator [65, 66]	Semi-empirical	Another relatively widely used tool developed by Zajic and Thieberger in Brookhaven National Laboratory. Based on an earlier version of SRIM with parametrization to experimental data measured by the developers. Available online at <a href="http://tvdg10.phy.bnl.gov/let.html">http://tvdg10.phy.bnl.gov/let.html</a> .
ECIF Cocktail Calculator [67]	Semi-empirical	Based on parametrization of modified Bohr's classical stopping theory [68]. Web interface can be found at <a href="http://research.jyu.fi/radef/ECIFcalc/dedx.html">http://research.jyu.fi/radef/ECIFcalc/dedx.html</a> .
PASS [69]	Theory	Based on the work by Sigmund and Schinner [70]. The calculations are fully based on fundamental physics without any parameterization to the experimental data. Stopping force values are available upon request from the model developers.
CaSP[71]	Theory	Convolution approximation for Swift Particles developed by Grande and Schiwietz and described in Ref. [101, and references therein]. Available online at <a href="http://www.casp-program.org/">http://www.casp-program.org/</a> .
Paul's database [72]	Data table	Extensive tabulation of published experimental stopping force data maintained by Helmut Paul. Available online at <a href="https://www-nds.iaea.org/stopping/">https://www-nds.iaea.org/stopping/</a> .
Hubert tables [73]	Data table	Tabulation of experimental stopping force values in the energy range from 2.5 to 500 MeV/u. Not as comprehensive as Paul's database above.

their pros and cons, and in cases where there is no experimental data to compare, it is in the user's judgement whether or not to rely on the values given by the predictor. Discussions have aroused among the radiation effects community about the differences in the estimated stopping force values between the tools especially for heavy ions like xenon [75]. This is due to the extrapolation of the parameters based on experimental data in other ion–target combinations.

### 1.3.8 Cumulative Effect: Total Ionizing Dose and Displacement Damage

Cumulative stress of radiation may cause gradual changes in the characteristic properties of electronics, such as threshold voltage shifts and decrease in the minority carrier lifetimes. There are two subdivisions for the cumulative effects: Total Ionizing Dose (TID) and Displacement Damage Dose (DDD). They are related to the concepts of the LET and the NIEL, respectively.

The TID effects are governed by those radiation-induced charge carriers, which have survived the recombination and are not swept away by the electric fields. Because the electron mobilities, especially in dielectrics, are higher than those of holes, typically the trapped charges are the holes. Moreover, the effect is more pronounced in dielectrics than in semiconductors. Although, in case of interface trapped charge, it is located in the semiconductor side of a dielectric–semiconductor interface. The TID effects can occur in both Metal–Oxide–Semiconductor (MOS) devices and bipolar devices. For more detailed information on TID effects, the reader is referred to Refs. [76, 77].

The DDD effects in electronics are induced by the NIEL associated with particle radiation (see Section 1.3.5). The atoms may get knocked out from their lattice site due to an ion hit, creating a vacancy–interstitial pair, called a Frenkel defect or pair (FP). Typically, the reduction in current gain of bipolar transistors or dark currents in CCDs are attributed to these defects. This work mainly focusses on the ionizing particle radiation, and the effects of NIEL or DDD are not discussed further.

### 1.3.9 Single Event Effects

The Single Event Effects (SEE) are referred to as the prompt response of electronics to ionization event, induced by a single energetic charged particle, as depicted in Figure 1.13. As discussed above, charged particles are capable of ionizing matter, i.e. generating e–h pairs in semiconductors and dielectrics. Typically, SEE occur when an ion strikes a reverse-biased PN junction in an off-state device, creating a transient, unwanted flow of current which may be sufficient to cause errors and/or physical damage. SEEs can be divided into two groups: non-destructive soft errors, and destructive hard errors. In the following sections, these two groups are briefly introduced.

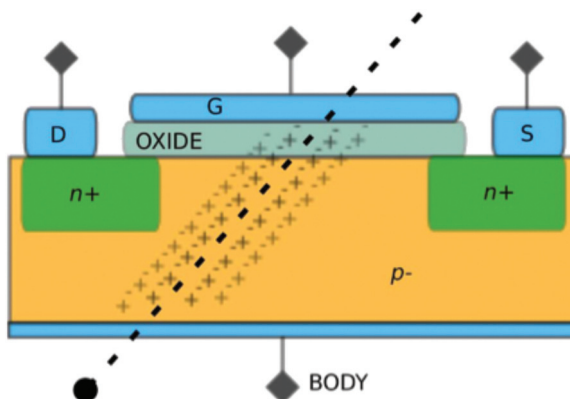


**Figure 1.13** A schematic view of an ion hit in an NMOS.

### 1.3.10 Soft Errors

When ion induces a temporary disturbance in an electronic circuit, which can be fixed by e.g. reprogramming the device, the effect is considered as a soft error. The main types of soft errors and their definitions according to Refs. [78, 79] are listed below.

Single-Event Upset (SEU) is an event where a memory bit (or bits) is (are) flipped, from 0 to 1 or vice versa. Typically, only one bit is affected at the time and the effect can also be called Single Bit Upset (SBU). In case of corruption of multiple bits, the event is referred to as Multiple Bit Upset (MBU), which can be a concern in highly scaled memories or with ion hits at high grazing angles. The basic principle of an SEU in an SRAM cell based on Complementary Metal–Oxide–Semiconductor (CMOS) technology is discussed below.

Single-Event Transient (SET) is a progressive disturbance in combinatorial logic systems caused by a single ion hit. The ramifications of an SET are dependent on e.g. the operation frequency of the circuit. SET may turn into an SEU, if it gets latched. In case of analogue devices (e.g. operational amplifiers, comparators and voltage regulators), the transient disturbance due to an ion hit is called Analog Single Event Transient (ASET). The faulty signal caused by an ASET can propagate in an integrated circuit and lead to significant anomalies, such as data corruption or system failure [22, and references therein].

Single-Event Functional Interrupt (SEFI) results in a loss of device functionality. After occurrence of SEFI, the malfunction can be fixed without

power cycling the device. SEFIIs are typically associated with SEUs in a control bit or in register.

Because the SEU is the “oldest” SEE-type, being observed in the first studies [13], it is chosen here as an example. The anatomy of an SEU in a typical SRAM cell is illustrated next.

The mitigation of these above-mentioned soft errors has become more important, not only in space electronics but also in general commercial electronics, due to the technological evolution [81]. The mitigation techniques can be applied either in circuit or software level. The reader is referred to Ref. [82] for a detailed discussion on different mitigation methods for soft errors in modern microelectronics, and they are also discussed later in this book.

### **1.3.11 Hard Errors**

In some cases, particle-induced “cloud” of e–h pairs may generate current peak in a device, which may initiate high currents, leading to a destructive failure. These kinds of irreversible hard errors are typically less probable to occur than the soft errors discussed above. Of course, their weight in radiation reliability of electronics is higher because once they occur, the device is partially or totally out of service. The typical destructive SEE types are listed below with short descriptions after Refs. [78, 79, 83]:

Single-Event Latch-Up (SEL) is potentially a destructive state in a device, where hit of a single ion creates conductive path between the device power supply and ground. The current through this path is stopped only by shutting down the power supply. The SEL may destroy the device if the current from the power supply is not limited and/or the power cycling is not performed fast enough after the current increase.

Single-Event Gate Rupture (SEGR) is a breakdown of gate oxide in MOS devices, attributed to ion-induced conductive path. The excessive current through the dielectric leads to material meltdown via thermal runaway. The basic physical mechanisms underlying SEGR are yet unknown, mainly because the rapid nature of the event impedes accurate measurement of the current spikes. Only some qualitative or semi-empirical models exist for SEGR prediction.

Single-Event Burnout (SEB) is a failure that can be observed typically in power devices (MOSFET or bipolar). In the SEB event, there is a highly conductive path created in lightly doped epitaxial layer of the device, which leads to excessive current, and ultimately to thermal runaway

with a permanent damage. In many cases, SEB and SEGR occur simultaneously in power MOSFETs.

Mitigation of SEL and SEB is possible by limiting the supply current of the device. The SEL is also possible to avoid by using Silicon-On-Insulator (SOI) technology [84]. However, SEGR is found to be impossible to avoid once the threshold conditions (oxide electric field and energy deposition density) are exceeded [83].

## 1.4 Effect of Radiation on Memory Devices

Ionizing radiation affects many types of electronic devices and, among them, memories are the most concerned by soft errors. According to the ITRS roadmap [Semiconductor Industry Association (SIA), “International Technology Roadmap for Semiconductors (ITRS); <http://www.itrs.net>], electronic memories are the dominant type of devices in embedded systems, representing the largest quota in Systems on Chip (SoC) area. Due to their rather simple architecture, compatibility with standard process and performances, memories are used in most computing systems. On the other hand, the inner characteristics of this type of device make them one of the main sources of errors in SoCs [85]. Moreover, the storage capability, that is, the main feature of all memories, makes them capable of storing radiation-induced errors, differently from combinational circuits where soft errors are less frequent and more difficult to detect.

### 1.4.1 Structure of a Memory

In order to ease the understanding of the interaction between ionizing particles and memories, it is useful to introduce the typical structure of a memory device. As depicted in Figure 1.14, memories are mainly composed of the memory cell array, where the data are physically stored, and peripheral circuitry which allows cell selection, data reading/writing, buffering and synchronization. Besides the memory cells, all the elements of peripheral circuitry may also be impacted by the radiation environment.

The memory array is not always composed of a single rectangular cell matrix, as seen in Figure 1.14, but it can also present more complex configurations such as the butterfly, with two cell arrays divided by a single row decoder [85], as depicted in Figure 1.15. This configuration reduces the word line length by half. At the same time, the bits of each word are split into two sub-arrays, with the row decoder physically dividing them.

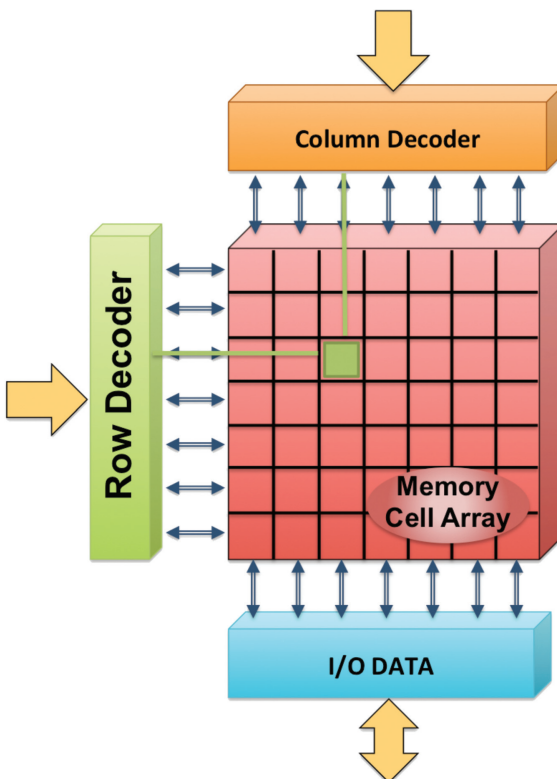


**Figure 1.14** Basic structure of a memory.

Simple or multiple arrays can be further organized into blocks, allowing the reduction of the size of bit lines and word lines, making the cell access (read/write) more effective and reliable, since the shorter wiring reduces delays. Another important feature of cell array is related to the size and location of the bits belonging to a memory word, which is generally made of between 8 and 64 bits. The cells corresponding to these bits are usually topologically distant, since interleaving schemes are applied. These schemes place all the bits belonging to the same word in different electric blocks, and the access to these bits during read/write operations are made through multiplexing structures. An example interleaving is given in Figure 1.16 that refers to a section of SRAM array, in which the cells are organized in  $4 \times 4$  blocks.

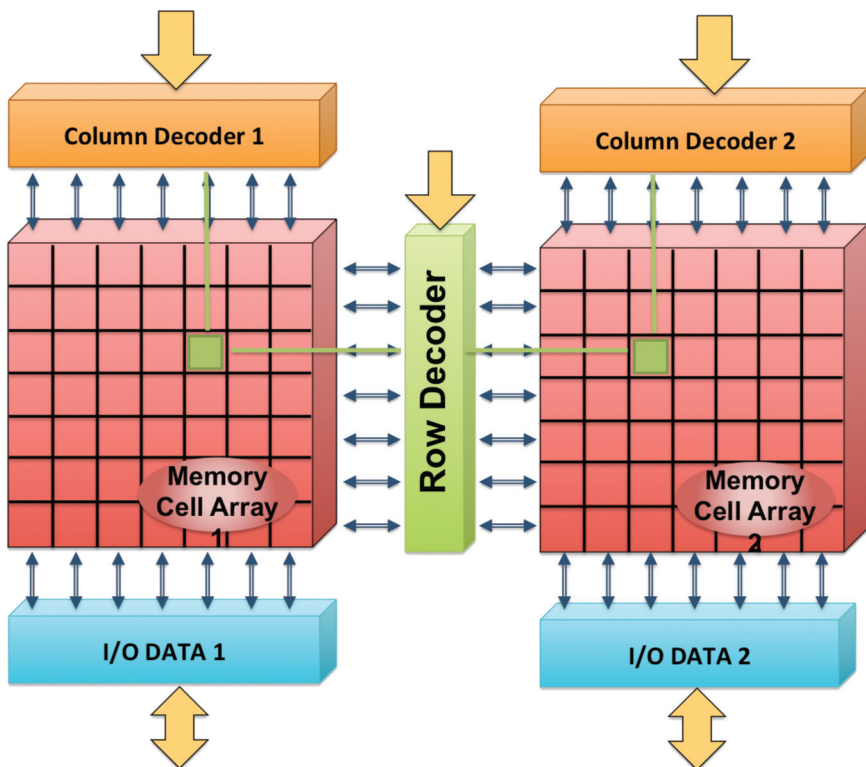


**Figure 1.15** Butterfly configuration of a memory.

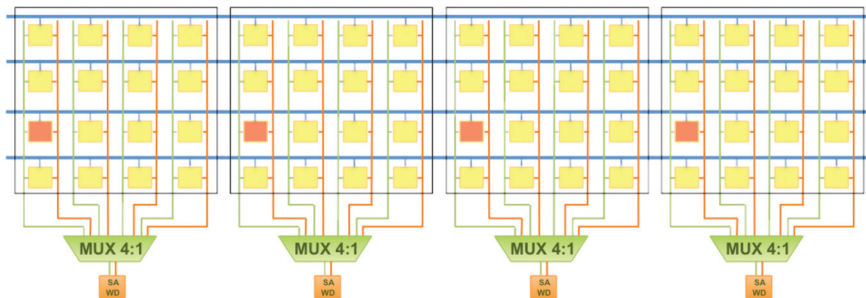


**Figure 1.16** Scheme of a section of an SRAM array organized in  $4 \times 4$  blocks.

The selection of a given word for a write/read access is done as follows:

- The word line that selects the given word is activated;
- Only one column per block is selected;

- The selected cells are connected to one read/write sense amplifier/write driver (SA/WD) unit through a 4:1 multiplexer.

In this configuration, the bits belonging to the same word are never topologically adjacent, but they are placed in separate blocks, with a minimum distance of three cells. In the case of blocks composed of  $16 \times 16$  cells, the minimum distance between two cells of the same word will be 15 cells.

In addition to interleaving schemes, scrambling techniques are also implemented in the cell array, thus contiguous values of addresses are generally not physically adjacent.

The main peripheral circuits are listed below:

- The **address decoders**, which allows selecting the row and column where to read/write;
- The **sense amplifiers**, which sense the state of the memory cells in order to convert it in binary form;
- The input/output (I/O) **buffers**, where the content of the fetched data is retrieved prior to latching the data on the I/O pins or wrapper;
- The **synchronization circuitry** ensuring that each action involved in the read/write action is performed within predetermined time constraints and in the correct order;
- The **write drivers** consisting of the logic elements used to force the logic values in the cells;
- The power and ground **grids** that feed the memory array as well as the peripheral circuitry;
- The **power switches** that allow switching ON/OFF parts of the circuit, especially in the case of low-power (LP) devices. For example, in LP SRAMs, power switches allow feeding the cells with different supply voltage values: low voltage ( $\sim 0.74$  V) to reduce leakage currents (and hence device power consumption), while still maintaining data retention; high voltage ( $> 1.1$  V) to allow read/write access without destroying the cell content during a read operation or failing the write of a cell due to the reduced write noise margin.

Depending on the considered type of memory and technology, the electrical and physical function of the device may change and require the use of specific circuitry and structures, such as charge pumps in flash memories, and a microcontroller and data buffers to control the I/O data exchange in large storage devices. In the following chapters, when needed, these specific structures will be presented and detailed, when needed to explain the introduced hardening techniques.

### 1.4.2 Classification and Fault Mechanisms in Memories

All malfunctions (related or not to ionizing particles) affecting any subcircuit of a memory are systematically mapped as error(s) in the memory array. These errors are in part actual bit flips and in part false bit flips, as in the case of read failures, in which although the selected cells store the correct data, the output data are incorrect. Based on these premises, the soft errors that affect memories can be classified as follows:

- Single Bit Upsets (SBUs) are generated when a particle-induced current flips the information stored in one memory cell (or a latch or Flip Flop in other types of circuit).
- Multiple Cell Upsets (MCUs) are special cases during which a single particle is responsible for the upset of more than one-bit cells. This phenomenon can be the result of a single particle nuclear reaction generating multiple recoils that travel at different directions depositing charge in multiple sensitive nodes, or the result of a single ion depositing sufficient amount of charge to upset two or more neighbouring cells [86].
- A special case of MCU is the Multiple Bit Upset (MBU), where more than one bit of the same word is corrupted. The application of interleaving schemes, introduced in the previous section, in the cell array (bit-cells of other words placed between consecutive bit-cells of the same word) makes MBUs unlikely to occur. Nevertheless, with the miniaturization of transistors - and consequently of bit cells, the probability of MBU appearance has increased in the recent years. This is mainly the result of the reduction of the distance between sensitive nodes, and the comparatively long range achieved by high-energy ions in silicon.

In order to show how ionizing particles may induce soft errors in memories, two examples of fault mechanism are introduced here, considering a single event affecting a memory cell (SRAM) and a peripheral circuit (address decoder). As introduced above, the resulting errors are mapped in the memory array, thus interpretable as error(s) in read bits.

***Example 1: Particle hitting an SRAM core cell.***

Considering the typical case of SRAM devices and the mechanism of indirect ionization, the fault mechanism can be explained as follows. The triggering event may be either:

- An energetic charged particle goes through the substrate of the target device, and ionizes target atoms along its path;

- An energetic neutron or ion impinges on a target atom within the device. Depending on the impinging particle energy and target atom isotope, a nuclear reaction can take place, possibly generating heavy ions as reaction products. These ions, retaining the momentum of the original impinging particle, will recoil in the silicon and ionize target atoms along their path;

In either case, a track of electron–hole pairs is created in the silicon. If such a track is generated close to a reverse-biased junction of an SRAM cell, the carriers will drift across the depletion region, creating a current spike [87]. The fast collection of carriers is completed within a few hundreds of picoseconds, while the collection takes place over a few hundreds of nanoseconds, until the carriers start to diffuse. Figure 1.17 illustrates the failure mechanism in an SRAM cell.

The parasitic current that is generated by the secondary ions occurring from the particle collision to the reverse biased junction of the drain of the NMOS transistor Mn4, is represented at the SRAM cell schematic with a current source. This current source discharges node SB (formerly at logic “1”, VDD), enabling the activation of transistor Mp3, thus leading to the complete flipping of the cell state (node S at logic “1”, node SB at logic “0”). This event can be the result of a neutron or high-energy proton impinging close to the junction. Alpha particles, heavy ions and low-energy protons, on the other hand, induce the parasitic current by traversing directly the silicon, leaving the electron–hole pair track on their path, resulting in a direct ionization mechanism.

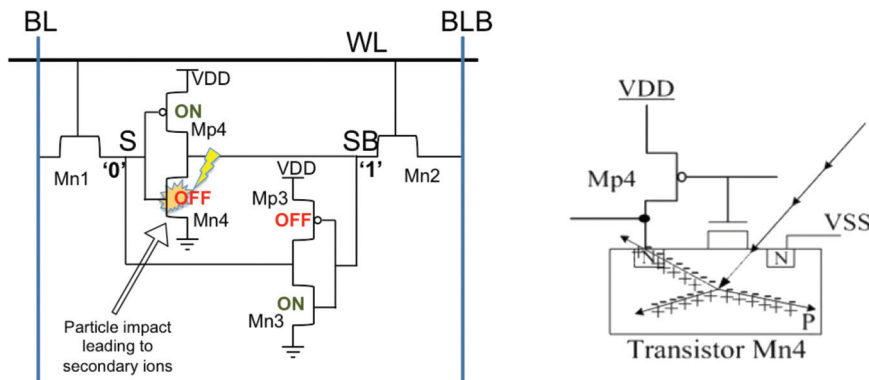


**Figure 1.17** SRAM cell fault model. A particle induces a nuclear reaction, which generates secondary ions. The ions create electron–hole pairs, which are drifted to the depletion region of the reverse biased junction of the drain of transistor Mn4.

When considering other types of memories, the fault mechanisms responsible for data corruption may be different, and will be detailed in the following chapters. For example, in a flash memory, the memory cell is composed of a floating-gate transistor, and the cell's stored logic value depends on the transistor's threshold voltage, hence, on the amount of charge stored in the floating gate. In this case, impinging ionizing particles may lead to data corruption by modifying this charge level, and/or cell state sensing through the accumulation of parasitic trapped charges in the transistor dielectric materials.

**Example 2: Particle hitting an SRAM address pre-decoder.**

This example shows how MBUs within the same word can be induced by temporary malfunction of the address decoder, as opposed to classic MCUs caused by a particle hitting the memory cell array. Figure 1.18 depicts the schematic of an address pre-decoder, which is composed of two stages. The first stage (on the left-hand side in the schematic) has synchronization function, with WLEN as a synchronization signal. The second stage (on the right-hand side) executes the decoding and amplification of the word/bit lines selection signals. For this example, SPICE simulations were performed considering a single ionizing particle hitting the first stage of the decoder, by using the charge injection model described in [88].

The injected charge induces an address decoder malfunction that provokes a double word line selection during a write operation. During a correct

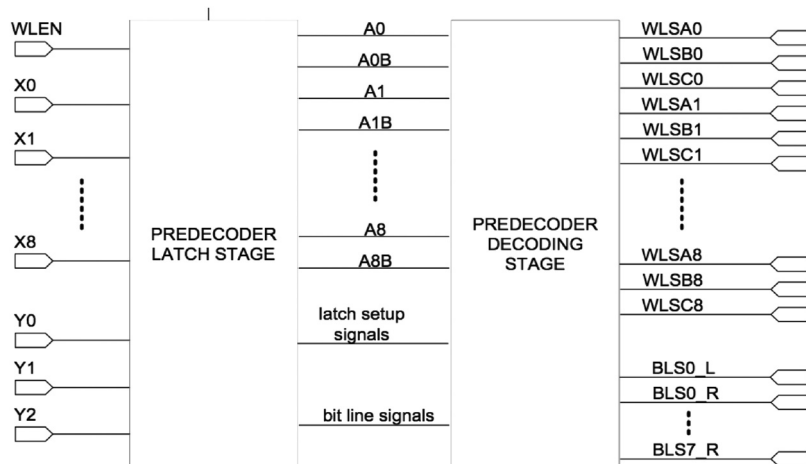


**Figure 1.18** Scheme of address pre-decoder.

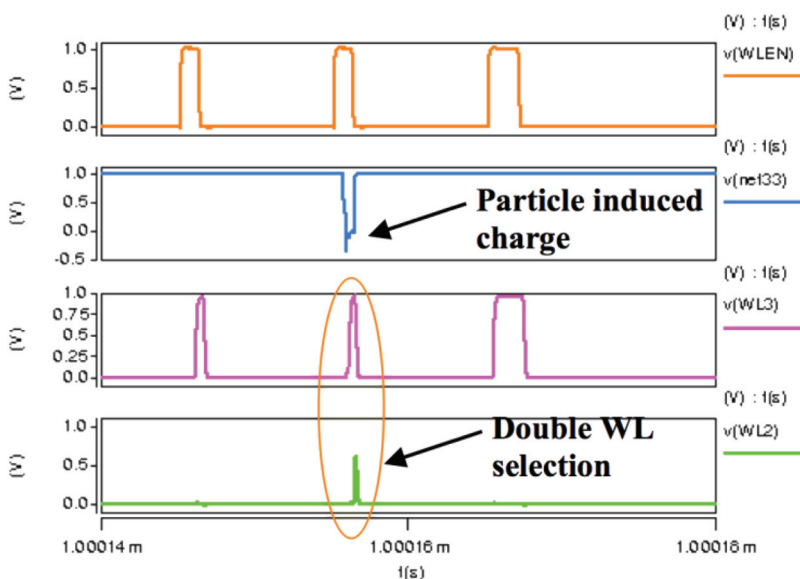


**Figure 1.19** Double word line selection during write operation.

address function, only a single word line (and thus a single word) selection per access is possible. Consequently, in case of faulty double word selection (due, in this case, to a particle hit) the data to be written are stored in the correct word (aggressing word) as well as in another one (victim word), potentially producing, in the latter, multiple bit flips. Figure 1.19 depicts this faulty behaviour: the word line signals WL2 (victim) and WL3 (aggressor) are activated at the same time. Considering an 8-bit victim word storing 00100101 before the faulty write, and the new stored data is 11111111; this introduces a 5-bit MBU (5-bit flips within the word).

Since address decoders are very similar, independently of the type of the memory, this same fault mechanism can be observed in several types of memory devices.

### 1.4.3 Memory Accelerated Tests

Functional and radiation-induced faults in an SRAM are either generated in the memory cell array, or are mapped in it. In other words, the error can be either generated in the core cell(s) and be observable with the cell read access, or be generated in the peripheral circuits and result in read/write failures or an access to wrong memory locations. These failures are next observed with read

accesses that only apparently reveal cell bit flips. For example, if during a read access, the synchronization circuitry is affected by a particle, the sensing time can be reduced. Consequently, the voltage difference between the two cell nodes to be sensed is reduced, and the value returned by the read operation is random, and thus potentially faulty. For an external observer, the error appears like a cell bit flip, although the cell still stores the correct value. In this case, a second read access will reveal whether the error is due to an actual bit flip, or to a failure in the access circuitry.

#### 1.4.4 Test Methods

Being the main process used for the qualification of electronic components in applications concerned with radiation effects, the accelerated test is a complex procedure that involves several parameters related to the device under test (DUT) and the environment of exposure. When it comes to evaluating a component's radiation sensitivity, the most important metrics are its cross-section (the area of the device that is sensitive to particle hits) and the minimum linear energy transfer (LET) threshold for impinging particles to cause an error. Although SRAMs are relatively simple components compared to Systems-On-Chip (SoCs) or microprocessors, their testing can hide several aspects that can affect their sensitivity estimation and need to be taken into consideration. Directives in the form of standards are given such as the JEDEC [89, 90], which provide fundamental guidelines for the testing of electronic devices. The guidelines that concern memories are mainly focused on static mode testing and display some complementary notes on dynamic mode testing. In the following paragraphs, the details and importance of each testing mode are analyzed, and various methods related to the dynamic mode test are presented.

Considering a simple level of abstraction, memory operation can be classified into two distinct modes: static mode (retention) and dynamic mode (read/write access). This abstraction is based on the major differences in the behaviour of the memory cells and controlling logic under these two modes. In static mode, memory cells perform data storage: the access transistors of the cell are OFF, and no interference on the cell is operated by normal function. When the cell is accessed for a read operation, the access transistors are activated, the stored logic value is determined by a sense amplifier, which returns either a logic “0” or a logic “1”. During a write operation, with the access transistor activated, the bit line(s) (properly set) force either the preservation or the flipping of the stored information in the cell. The activation

of the peripheral circuitry of the memory (address decoders, write drivers, pre-charge circuitry, etc.), the electric weakening of the cell (due to the read access in some types of memories like SRAMs) and other phenomena, typical of dynamic operation mode, do not occur in static operation mode. Conversely, when in static mode, the cell is in retention, which for many cases (especially for low-power SRAMs) means that the voltage in the memory array approaches its threshold limit reducing the static noise margin of the cell. These differences make the cells more or less susceptible to Single Event Upsets (SEUs) such as SBUs, MCUs, MBUs and Single Event Functional Interrupts (SEFIIs). Consequently, it is essential to differentiate the modes of testing, depending on the level of SEU sensitivity of the memory in Static and Dynamic modes.

#### **1.4.5 Static Mode Testing**

Static mode testing is one of the most fundamental testing methods for the vast majority of memories, and especially SRAMs. It is described as the key test method by various standards, and it requires the writing of the memory with a known data pattern prior the exposure to the radiation source (natural/real-time, accelerated, etc.). Following the exposure of the memory under radiation for the time or scheduled fluence, the memory is read back to check for possible bit-flips. The data background must be stored on the memory prior to the irradiation, in order prevent “dynamic” errors during the initializing (writing) process.

Static mode testing has a major benefit, which is the rather stable response of the memory in terms of sensitivity. Since the only part of the memory that is affected is the cell array and not the periphery, all errors are classified into two major categories, which are easy to distinguish and define the error probability, as opposed to the dynamic mode testing that has several different sources and types of errors. The two major categories of errors are SBUs and MCUs. An SBU occurs when a particle impinging the memory cell array induces a parasitic charge through either direct ionization (heavy ions, alphas, low-energy protons) or indirect ionization (neutrons, protons), and this charge flips the bit stored inside one cell. An MCU, on the other hand, is the result of the same phenomenon, with the difference that the parasitic charge affects multiple cells that are topologically adjacent in the memory array.

During static mode testing, the choice of the data pattern depends on the type of test and the depth of analysis that needs to be achieved. Typical sets of data backgrounds are the following ones: solid 1 (all “1”s), solid 0 (all “0”s),

checkerboard (“10101010”) and inverse checkerboard (“01010101”). Comparison between the solid 1 and solid 0 data patterns can reveal the relation of the stored information (logic “1” or “0”) with the sensitivity of the cell, as a result of intra-die variations, or resistive/bridging defects within the cells or the memory array. Checkerboard and inverse checkerboard may reveal differences in the overall response of the memory array, as well as differences regarding the shapes and sizes of MCUs, as shown in [91].

### 1.4.6 Dynamic Mode Testing

Although in the various standards describing radiation testing a basic methodology is provided for the dynamic mode testing of memory devices, no detailed guidelines are given, and moreover, no special cases are taken regarding the memory under study and its respective technology. Such guidelines cannot cover all types of memory devices when operating in dynamic mode, because each type of device has its own sensitivity that also depends on the access pattern (sequence of read/write operations). A certain access pattern may stimulate (stress) one device and leave another one without any stress effect. As mentioned above, when the memory operates under static mode, only the cell array is susceptible to SEEs, while when in dynamic mode, other types of SEUs may occur besides typical SBUs and MCUs such as SEFIs and SELs: additional regions of the memory are activated, and thus become vulnerable to impinging particles. For example, the injection of a parasitic current in the address decoder during a write operation may result in storing data in wrong memory locations, as shown in the example given in Section 1.4.2.

Finding the proper testing scheme to stimulate a memory device under its typical, best-case or worst-case scenarios is not evident when operating in dynamic mode. March algorithms are currently used in the manufacturing process because they are capable of detecting faults in memory devices, such as bridging faults, stuck-at faults and coupling faults among others. They are preferred for their efficiency and low complexity. Depending on the type of memory, different algorithms are preferred based on their efficacy, thus, some algorithms are expected to be applied for SRAMs and different ones for other types of memories such as DRAMs and FLASH. Since March algorithms are able to stimulate the memory devices in order to reveal manufacturing defects, providing a suitable functional test, they become the perfect candidate for radiation dynamic testing, as they can be tuned to operate the typical as well as the worst-case scenarios of the memory’s operation.

**Table 1.2** Marching test algorithms

Name	Test
March C-	$\{\uparrow(w0); \uparrow(r0,w1); (r1,w0);$ $\downarrow(r0,w1); \downarrow(r1,w0); \uparrow(r0)\}$
Mats+	$\{\uparrow(w0); \uparrow(r0w1); \downarrow(r1w0)\}$
mMats+	$\{\uparrow(r0w1); \uparrow(r1w0)\}$
Dynamic Stress	$\{\uparrow(r1,w0,r0,r0,r0,r0);$ $\uparrow(r0,w1,r1,r1,r1,r1);$ $\uparrow(r1,w0,r0,r0,r0,r0);$ $\downarrow(r0,w1,r1,r1,r1,r1);$ $\downarrow(r1,w0,r0,r0,r0,r0);$ $\uparrow(r0,w1,r1,r1,r1,r1)\}$
Dynamic Classic	$\{\uparrow(w0); \uparrow(r0); \uparrow(w1); \downarrow(r1)\}$

Table 1.2 shows a list of the March algorithms introduced in various works by the authors, such as the Dynamic Stress (March DS), the March C- and the Dynamic Classic among others.

Each March algorithm is made of several elements. Each element entails a series of operations (read or write). Each element has a given addressing order of execution: the arrow at the beginning of each element indicates the order of the addressing, i.e. from the highest memory address to the lowest ( $\downarrow$ ), or from the lowest to highest ( $\uparrow$ ). The operations of each element are all applied to each address location (word), before proceeding to the next address. This means that all the operations of the element are applied to a single word, before the address counter of the tester is increased, or decreased, depending on the direction ( $\uparrow$  or  $\downarrow$ ) of the element. A semicolon separates the elements of the algorithms and each element has its operations enclosed in brackets. For example, the fourth element of March C-  $\downarrow(r0, w1)$ , has an addressing scheme starting from the uppermost address towards the lower ones, and applies a “read ‘0’” followed by a “write ‘1’” operation into all the memory locations. This means that the tester reads a single word and expects to receive a zero pattern, after which it writes all the bits of the same word with logic “1”. Once these two operations are finished, the tester proceeds to the next word, and applies the same pattern.

For all the algorithms in Table 1.2, the data background stored and read from the memory is either a solid “0” or a solid “1” and the swapping from “0” to “1” (or the opposite) stresses (by increasing the switching activity) some peripheral circuitry of the memory such as the I/O buffers. Other parts of the memory can be stressed as well such as the address decoders by using the specific techniques. For example, the address decoder can be stressed by

applying an addressing sequence in which most of the bits change at each access, strongly enhancing the switching activity of the address buffer and decoders, as explained in [85].

Depending on the given March algorithm, a strong stress factor can be induced to the memory such as the cases of March Dynamic Stress (DS) for SRAMs, while others like the Classic are less stressful, when not properly modified. As demonstrated in [92], the algorithm March DS induces a stress to the SRAM cell by applying sequences of read operations in the same locations. When sequentially made, the read operations reduce progressively the static noise margin of the cell by degrading the voltage level of the nodes. As explained in [93], the March DS algorithm, which is proven for the SRAMs to be amongst the most stressing algorithm, has the opposite impact on FRAMs. Considering this example, it becomes clear that each type of memory has its own particularities, which need to be well analyzed before structuring a test methodology.

In order to enhance or reduce furthermore the stress of the memory array and the periphery, some additional properties of March test algorithms are detailed in [94], such as Fast Row; Fast Column; Random Addressing; Adjacent (Gray) Addressing and Inverse Gray Addressing. These complementary techniques to already existing March algorithms affect the level of electric stress induced to the address decoders, the data buffers and other peripheral circuitry by playing on the address order and the data background.

## 1.5 Radiation Hardness Assurance Testing

There are various particle radiation sources present at the ground level and in space. The radiation hardness of electronics operating in harsh radiation environments, such as nuclear power plants, accelerators or in space, needs to be assured either by manufacturing them with radiation hardness in mind, or by testing them. In earlier days, there were dedicated manufacturers for rad-hard components, which were competitive in performance with commercial products. When the Cold War ended and the rivalry over space supremacy cooled down, the production of rad-hard electronics was no longer a prosperous business. Only a few manufacturers remained in the field, none of them exclusively on rad-hard products. Because of high production costs, nowadays the rad-hard industry is mainly focused on parts with high reliability requirements. In addition to lower prices, the performance of commercial electronics (COTS, commercial-of-the-shelf) is typically much higher than that of rad-hard devices. Thus, COTS devices are often favoured in space

projects due to superior performance and low cost; however, the drawback is their lack of being space qualified and unknown radiation performance.

As said, to ensure the radiation hardness of an electronic component which was not manufactured rad-hard, the component needs to be tested under radiation. There are some requirements for these Radiation Hardness Assurance (RHA) tests, set by the radiation effects community. Some of the most commonly used specifications are presented in Refs. [78, 95–97]. These documents determine the framework within which RHA tests typically need to be performed. As the aforementioned particle radiation environments are dominated by light particles (i.e. protons and electrons), the total dose issue is the first to be considered. Due to the focus of this work, which is on particle radiation and particularly on heavy ions, the total dose testing is not discussed further. Instead, an introduction on the basics for RHA testing for SEEs is given.

The radiation environment is usually represented by its LET spectrum, which is considered to represent a particle's ionizing power. This can be done by first defining individual particle spectra (see Figure 1.4) in terms of their LET and merging them together. The result is a single spectrum representing the given environment. As an example, four LET spectra are presented in Figure 1.20, where radiation environments in two different regions are estimated during solar maximum and minimum (the data are taken from Refs. [10, 99]). Because of the presence of heavy ions (or high LETs) in these environments, not only the total dose effects are a concern, but the electronics need to be determined also for their susceptibility to SEE. In principle, SEEs can be produced by any source emitting particle radiation, but the particles must have sufficient energy to penetrate into the device all the way down to the silicon, and be able to generate enough ionization. In addition, the used radiation needs to mimic the effects in the real operational environment.

In laboratory, radiation sources, such as Ra-226 ( $\sim 100\%$   $\alpha$ -emitter, with some gamma radiation) and Cf-252 ( $\alpha$ -emitter, with 3% of spontaneous fission, producing also neutrons) [100] are convenient for this purpose because of their relatively low price and ease of use. The disadvantage in these sources is the limited ion energies and species as well as the limited particle flux. Furthermore, there may be more than one particle type, emitted at several different energies from the source. Also, radiation type may be multifaceted, e.g. including also gamma or neutron radiation, which limits the usefulness of these sources even more. Due to these limitations, the use of radioisotope sources is prohibited in the official RHA tests by the specifications [78, 95]. These sources are typically used only for trial runs of the setup for the

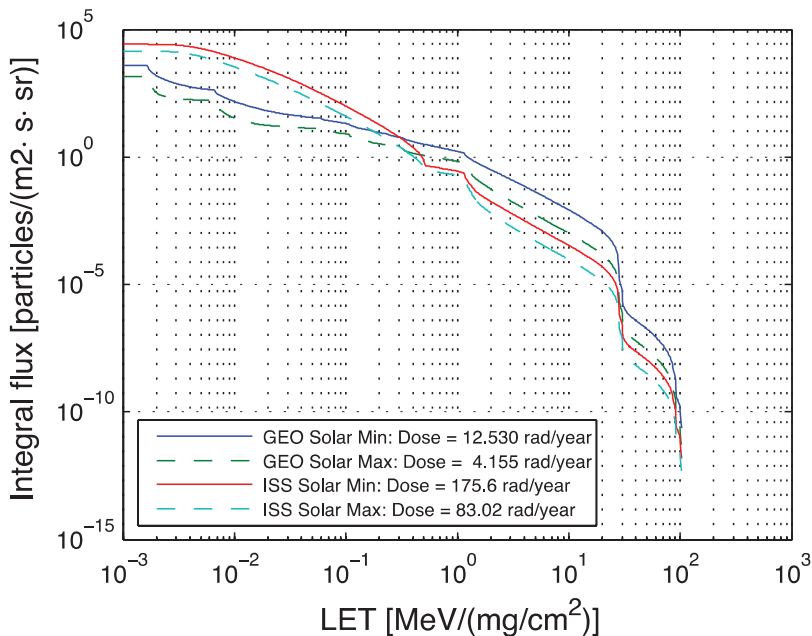


**Figure 1.20** Integral flux of galactic cosmic ray particles during solar minimum (solid) and solar maximum (dashed) as a function of Linear Energy Transfer in GEO or near Earth interplanetary space (blue and green) and International Space Station orbit (red, cyan). Data taken from [10]. Figure taken from Ref. [4].

RHA testing. The specifications for RHA testing for SEEs require the use of particle accelerators.

The particle accelerators are multi-purpose tools, which in the past have been used mainly in basic nuclear physics studies. In recent years, accelerators have been increasingly used for applied research, such as RHA tests. Next, a short introduction is given on the basic principle of SEU testing using heavy ions.

As discussed above, SEUs are the most prominent error type in electronics. SEU testing of e.g. memory devices is done by irradiating a memory with certain ions (each ion species yielding a maximum LET in a given target material), at fluences ranging from  $10^6$  to  $10^7 \text{ cm}^{-2}$  depending on the device sensitivity [78, 95]. Typically, above the sensitivity threshold, more than 100 upsets are required to obtain adequate statistics. The required ion fluxes are from  $10^2$  to  $10^5 \text{ cm}^{-2}\text{s}^{-1}$ . In a typical test procedure after the ion exposure, the memory is read and the number of bit flips (SEUs),  $N_{err}$ , are

determined. From this, the SEU cross-section per bit can be calculated by using the equation:

$$\sigma_{SEU} = \frac{N_{err}}{n_{bit} \cdot \Phi}, \quad (1.14)$$

where  $n_{bit}$  is the number of bits in the tested memory and  $\Phi$  is the ion fluence given in  $\text{cm}^{-2}$ . By changing the LET (using different ions), the characteristic SEU sensitivity of a device can be obtained. Moreover, the LET can be varied by tilting. This introduces a concept of effective LET which is defined as:

$$LET_{eff} = \frac{LET}{\cos(\theta)}, \quad (1.15)$$

where  $\theta$  is the angle of incidence for the impinging ion, and LET is the electronic stopping force of the ion. By definition,  $\theta = 0^\circ$  when the ion trajectory is perpendicular to the device surface. The applicability of the effective LET has also been questioned over the years, along with the concept of LET in general (see discussion above). No further comments will be made on the suitability of the effective LET concept here. One should also note that under tilted conditions the ion fluence,  $\Phi$ , should be replaced by the effective fluence:

$$\Phi_{eff} = \Phi \cdot \cos(\theta), \quad (1.16)$$

In Figure 1.21 are SEU cross-section data for an SRAM plotted against (effective) LET. This is a typical way to characterize the radiation susceptibility of electronics. In this plot are data measured in three different facilities: the Heavy Ion Facility (HIF) in Louvain-la-Neuve, Belgium [91], the Radiation Effects Facility (RADEF) in the University of Jyväskylä [102] and the Radiation Effects Facility in the Texas A&M University, USA [93].

This kind of characteristic plot can be used to estimate the SEU rates in the operational environment. This can be done by using a dedicated software, e.g. CREME- 96 [10], by assigning the environment and entering the parameterized SEU cross-section curve. From these input data, the code will give an estimation for the SEU rate in orbit. A very good demonstration of this procedure is given in Ref. [104], where one of the studied devices is the 4 Mbit Atmel AT60142F SRAM, discussed above. The agreement reported in this chapter between estimated and observed SEU rates is fairly good.

### 1.5.1 Beam Requirements

As mentioned in the previous sections, the radiation source used for a particular radiation test must fulfil a certain set of requirements, which depends

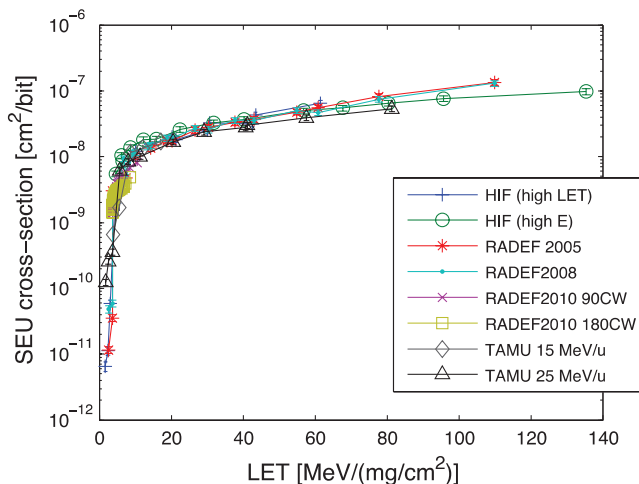


**Figure 1.21** SEU cross section for 4 Mbit Atmel AT60142F SRAM used in the SEU monitor [52]. Figure taken from Ref. [4].

on the type of test to be carried out. The following subsections give a brief summary of the ESA ECSS requirements for parts qualification in TID, TNID and SEE tests. The dose level or fluence level required to qualify a part is generally dependent on its intended mission.

### 1.5.2 TID Tests

TID tests are generally carried out with electrons or gamma rays; the ESA ESCC Basic Specification No. 22900 [105] indicates that TID tests may be carried out with either cobalt-60 gamma rays (two peak photon energies at 1.17 MeV and 1.33 MeV, with a low-energy tail) or with steady-state electron irradiation at an energy of at least 1 MeV at the sensitive volume. At these energies, photons and electrons have the advantage of high penetration (the typical component thickness is much smaller than the attenuation length/path length) and do not cause considerable displacement damage.

The dose rate can be adjusted to meet the required dose level in a reasonable irradiation time – ESCC specifications allow a range of 36 rad/h to 180 krad/h. However, the selected dose rate must take into account an eventual enhanced low dose rate sensitivity (ELDRS) [106] of the tested device. The irradiation must be carried out at room temperature and can be carried out in air.

### 1.5.3 TNID Tests

Currently, no standard method exists for TNID testing. However, ESA standards ECSS-Q-ST-60-15C and ECSS-E-HB-10-12A recommend that TNID tests be carried out with protons, at several different energies, up to 200 MeV, for a total TNID level of  $2 \cdot 10^{11} \text{ cm}^{-2}$  50 MeV equivalent proton fluence. The equivalent 50 MeV proton fluence can be calculated with the methods described in [107–108].

### 1.5.4 SEE Tests

Single Event Effects tests are carried out using protons and heavy ions. According to ESCC Basic Specification No. 25100:

- Proton SEE testing must be carried out using several different energies, ranging from a few MeV (to check sensitivity to direct proton ionization) to 200 MeV. Ideally, the source should be able to deliver a variable particle flux in the range of  $10^5 \text{ cm}^{-2} \cdot s^{-1}$  to  $10^8 \text{ cm}^{-2} \cdot s^{-1}$ . It is recommended to check the sensitivity of the DUT to the beam incidence angle.
- Heavy-ion testing must be carried out using ions with a range of at least  $40 \mu\text{m}$  in silicon, with a variable flux ranging between a few tens of  $\text{ions} \cdot \text{cm}^{-2} \cdot s^{-1}$  to  $10^5 \text{ ions} \cdot \text{cm}^{-2} \cdot s^{-1}$ . Ideally, the irradiation should be performed in vacuum to avoid degrading the beam spectrum, and the ion energy should be selected so that the Bragg peak is located at the depth of the device's sensitive layers.

### 1.5.5 Sample Preparation

Depending on the radiation type and energy to be used during testing, sample preparation steps may be necessary to allow an adequate energy deposition profile within the device.

### 1.5.6 TID Tests

In thin target devices, the secondary electrons generated by the primary electron beam may have sufficient energy to escape the target material, resulting in a loss of energy from the target and in a reduction of the effective deposited dose. To counter this effect, it is recommended to surround target devices with material providing charged-particle equilibrium during irradiation.

In the case of cobalt-60 irradiation, the upper layers of the device may receive a higher dose because of the low-penetration, low-energy tail of the cobalt-60 gamma spectrum. To mitigate this effect, it is advisable to surround the target device with a container of at least 1.5 mm of lead, with at least 0.7 mm of aluminium lining [105].

### 1.5.7 SEE Tests

SEE tests carried out with low-penetration beams (e.g. heavy-ion and low-energy proton beams) must be carried out on “opened” packages, to minimize the amount of material in the beam’s path – thereby minimizing the energy spread of the beam. Package opening is generally performed via a combination of mechanical and laser ablation, and chemical etching. It is a delicate operation, because the device must remain functional after opening – meaning that the delicate chip features must not be damaged, in particular the thin bonding wires connecting the die to the package pins.

SEE tests carried out with high-penetration beams (e.g. neutron and high-energy proton beams) may be carried out on non-opened devices.

### 1.5.8 Radiation Facilities

Introducing different European facilities for radiation effects studies as of 2018. Discussing in detail the RADEF facility of University of Jyväskylä, Finland.

### 1.5.9 ESA European Component Irradiation Facilities (ECIF)

The European Space Agency supports four European Component Irradiation Facilities (ECIF) to perform its radiation hardness testing:

- The Radiation Effects Facility (RADEF), at the University of Jyväskylä(Finland), can provide a variety of particle beams [109]:
  - heavy-ion beams from nitrogen to xenon, at energies from 4 to 9.3 MeV/amu (for a surface LET in silicon ranging from 1.83 to  $60.0 \text{ MeV} \cdot \text{cm}^{-2} \cdot \text{mg}^{-1}$ );
  - proton beams from about 500 keV to 50 MeV;
  - electron beams at 6, 9, 12, 16 and 20 MeV;
  - continuous spectrum X-ray beams – either from 0 to 6 MeV, with a peak around 1 MeV, or from 0 to 15 MeV, with a peak around 2 MeV.

- Several facilities at the Université Catholique de Louvain (UCL, Belgium):
  - the Heavy Ion Facility (HIF), which provides ions from carbon to xenon (for a surface LET in silicon ranging from 1.3 to  $62.5 \text{ MeV} \cdot \text{cm}^{-2} \cdot \text{mg}^{-1}$ );
  - the Light Ion Facility (LIF), which provides a 65 MeV proton beam, which can be degraded down to about 10 MeV;
  - the Neutron Irradiation Facility, which provides continuous-spectrum secondary neutron fields;
  - a cobalt-60 source for TID testing.
- The Proton Irradiation facility (PIF, Paul Scherrer Institute, Switzerland) [110], which delivers proton beams from 6 to 230 MeV
- The cobalt-60 irradiation facility at the ESA European Space Research and Technology Centre (ESTEC), which can be used for TID testing.

### **1.5.10 Other Outstanding European Facilities**

Among the main European accelerator facilities used for space radiation physics are:

- The UNILAC linear accelerator and SIS-18 synchrotron at the Gesellschaft für Schwerionenforschung (GSI, Darmstadt, Germany), which can deliver a wide variety of heavy-ion beams ranging from 1 MeV/amu to 1 GeV/amu. The low-energy ions from the UNILAC can be collimated down to a 10  $\mu\text{m}$  diameter spot for spatially resolved radiation hardness studies.
- Several facilities at the Grand Accélérateur National d’Ions Lourds (GANIL, Caen, France), which together can accelerate heavy ions from carbon to lead at energies ranging from below 1 keV/amu up to 100 MeV/amu, generating LETs in silicon from below 1 up to  $100 \text{ MeV} \cdot \text{cm}^2 \cdot \text{mg}^{-1}$ .
- The U-400M cyclotron of the Joint Institute for Nuclear Research (JINR, Dubna, Russia) can accelerate ions from lithium to bismuth at energies ranging from 3 to 40 MeV/amu, generating LETs in silicon from about 1 to  $100 \text{ MeV} \cdot \text{cm}^2 \cdot \text{mg}^{-1}$ .
- The ChipIR facility at the ISIS Neutron and Muon Source (Rutherford Appleton Laboratory, Didcot, UK) is a beamline dedicated to the study of SEEs in microelectronics, using an atmospheric-spectrum neutron beam.

### 1.5.11 Other Outstanding Facilities in the World

- The 20-ID-B2 beamline at the Advanced Photon Source (APS, Argonne National Laboratory, Chicago, USA-IL) and the VESPERS beamline at the Canadian Light Source (CLS, Saskatoon, Canada) can deliver pulsed, focused X-ray beams for SEE testing. This is similar to laser SEE testing, with the added benefit that unlike laser light, X-rays can penetrate the metal layers covering the sensitive volumes in highly integrated ICs.
- The BASE facility at the 88-inch Cyclotron (Lawrence Berkeley National Laboratory, Berkeley, USA-CA) is specialized in radiation effects testing. It can provide neutron beams from 8 to 30 MeV, proton beams from a few MeV to 55 MeV, and heavy ions from helium to bismuth, at energies between 4.5 and 30 MeV/amu, generating LETs in silicon between 0.1 and 100  $\text{MeV} \cdot \text{cm}^2 \cdot \text{cm}^{-1}$ .
- The Crocker Nuclear Laboratory (University of California Davis, Davis, USA-CA) has been studying the effects of space radiation on electronics since the 1970s; its 76-inch cyclotron can provide proton beams from 4 to 67.5 MeV, in addition to neutron and alpha beams.
- The Radiation Effects Facility at the Texas A&M University (TAMU, College Station, USA-TX) was designed to irradiate electronics components with ions ranging from helium to gold at energies between up to 40 MeV/amu, yielding surface LETs in silicon between 0.11 and 82  $\text{MeV} \cdot \text{cm}^2 \cdot \text{mg}^{-1}$ . It can also deliver proton beams up to 40 MeV.
- The Proton Irradiation Facility (PIF) and Neutron Irradiation Facility (NIF) at TRIUMF (Vancouver, Canada), which can be used for high-energy proton and atmospheric-spectrum neutron SEE studies.
- The Single Event Effects Test Facility (SEETF) at the Michigan State University, which can be used for heavy-ion SEE testing [111].
- The Single Event Effects test facility at Oak Ridge National Laboratory, which can be used for high-energy proton testing of large equipment [112].

### 1.5.12 Accelerated Test for Memories

In the following part of this chapter, experimental results from radiation testing campaigns using different types of particle accelerators will be given and analyzed. Before exposing these results, it is important to describe some details on experiment configuration during the test of memory devices.

### 1.5.13 Memory Test Setup

The accelerated test on memories can be carried out to explore the effects of TID or the occurrence of single events. The TID tests do not require the monitoring of the device during the irradiation phase, but rather measures or functional tests that can be periodical operated when the device is not irradiated. The test of memories for single events, especially in dynamic mode, requires a continuous monitoring. For this purpose, a test setup similar to the one depicted in Figure 1.22 must be used. In this setup, the chip to be irradiated is mounted on a dedicated PCB card and controlled by a tester board via cables that are long enough to keep the tester outside of the beamline. Such a setup is chosen to assure the correct functionality of the tester during irradiation. The Tester board has a Field Programmable Gate Array (FPGA) as the main processing and communication unit, which the test firmware is implemented. FPGAs are chosen as testers more often than microcontrollers, thanks to the reliability of their operation flow, and the possibility of complete control over the timing of execution of operations, among other benefits. Both the tester board and the memory board are powered with power supplies that are located in the control room (or at least driven from it), in order to be able to power them off in case of a persisting SEL.

When it comes to static mode testing, the test firmware writes the data background sequence to the memory device prior to irradiation. After the beam exposure, it reads the data back, and compares them to the initial data

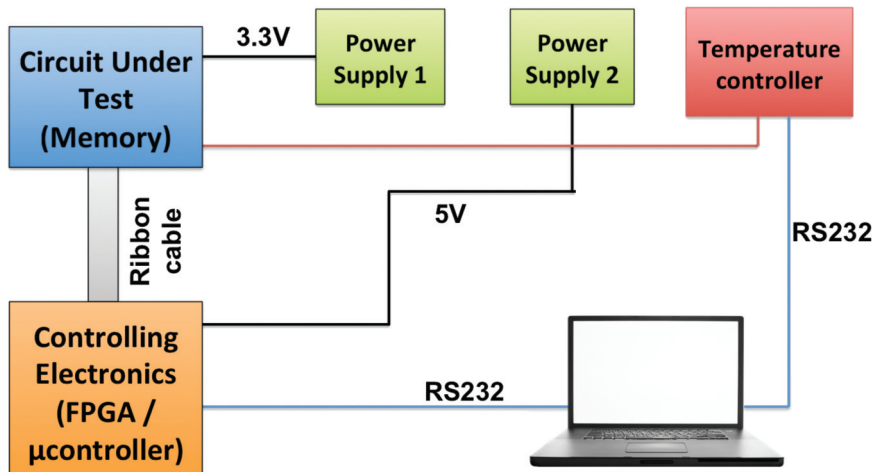


Figure 1.22 General scheme of irradiation test setup for memories.

pattern. In case of an error, the tester sends to the control computer all the necessary information for data processing. More specifically, the message is composed of an initiating sequence that indicates the code of the device, the address of the erroneous word, the erroneous word and finally information regarding the applied test. In the case of static mode test, the expected data background is sent, while in the case of dynamic mode test, made through March algorithms, the element and operation at which the error was located is given (e.g. the third element and the first operation of the March C- algorithm, “r1”, see Table 1.2), as well as the timestamp of the error occurrence.

One of the essential parameters for the data processing of the observed SEUs is the knowledge of the scrambling algorithm of the memory. Without the knowledge of the actual physical location of the SRAM cells in the memory array, it is very difficult not only to distinguish between SBUs and MCUs, but also to understand the origins of larger events occurring during dynamic mode testing such as SELs and SEFIs.

Adapting March algorithms for the purpose of radiation testing is a straightforward process. The tester needs to implement a Finite State Machine (FSM) which, depending on the algorithm, applies the required operations and elements to the memory under test. Besides the stimulus action, the read operations of the March algorithm work also as verification elements of the test, since the read pattern is compared with the expected one. For example, for a March element like  $\downarrow(r_0, w_1)$ , the read “0” operation will read the contents of an SRAM word, and will compare them to a “golden reference” word with all its bits being “0”’s. In case of an upset, a message described earlier will be transmitted to the control computer. For both the static and dynamic mode tests, it is imperative to record all addresses and contents of the failing words, and not to use an internal counter when testing SRAMs for the aforementioned reasons of detecting and identifying MCUs, SEFIs, SELs and other large-scale events.

Although stimulating the memory by using various testing techniques is one of the most important parameters to be considered when performing radiation testing, it is not the only factor that can affect the sensitivity of the device. Temperature variations can have an effect, either increasing or decreasing their performance. In order to achieve temperature variations when placing the memory devices under the beam, a complementary part of the setup is the temperature controller. A feedback loop composed of a foil heater, a thermocouple as a temperature sensor and a controlling instrument can be used to achieve high temperature variations. The sensor would provide the current temperature to the controlling instrument, which would

increase or decrease the input current to the foil heater to achieve the target temperature. Low temperature variations can be achieved by inserting the memory in a cryogenic chamber filled with argon gas that allows decreasing the temperature below 0°C, preventing the condensation of water vapour on the electronic devices. With a foil heater, a temperature sensor and a control instrument, the desired temperature is achieved.

Depending on the energy of the particles used to test the memory, the die of the device may need to be directly exposed, to avoid excessive energy straggling or even complete attenuation of the beam before reaching the silicon. When it comes to heavy ions or low-energy proton testing, the DUT is inserted into a vacuum chamber, and it is often necessary that the top part of the packaging is removed (an operation referred to as “delidding”). In order to be able to change the device in a relatively easy manner when the dose levels are high, a chip socket is used to hold the chip.

#### 1.5.14 Notes on Test Result Analysis

Regarding the irradiation of semiconductor memories, the primary result that is generally analyzed is the cross-section of the device, as was introduced earlier in this chapter. The calculation of the cross-section is done using the number of upsets observed in the memory and the total particle fluence per unit area. Nevertheless, it is important to note that a single-event may either lead to one Single-Bit Upset, or to several bit flips (Multiple Cell Upset). Thus, it is important to distinguish a **raw-cross section**, which considers each bit flip in the computation, and an **event-cross section**, which considers only the event count (each event causing one or more bit flips). This concept is well understandable when the test bitmap of the irradiated memory is analyzed. An example is given by the bitmap depicted in Figure 1.23, which was generated from the results of heavy-ion dynamic test irradiation on a 90 nm, 32 MB SRAM from Cypress Semiconductors. Several small patches and a few large bands are visible, where the data have been severely corrupted. A detailed analysis of these different types of error clusters is available in [113], which will be briefly reported here. The smallest patches, barely visible, have been caused by direct heavy-ion ionization (type A). The small horizontal patches were caused by limited micro-latch-ups (type B). The wide horizontal bands were very likely caused by a failure of the I/O data buffers (type C), and the wide vertical bands on the edges of the die were probably caused by a failure of the power switches (type D).

Provided that the memory has not suffered too many upsets during a test (the physical bitmap does not exhibit too many sparse black pixels),

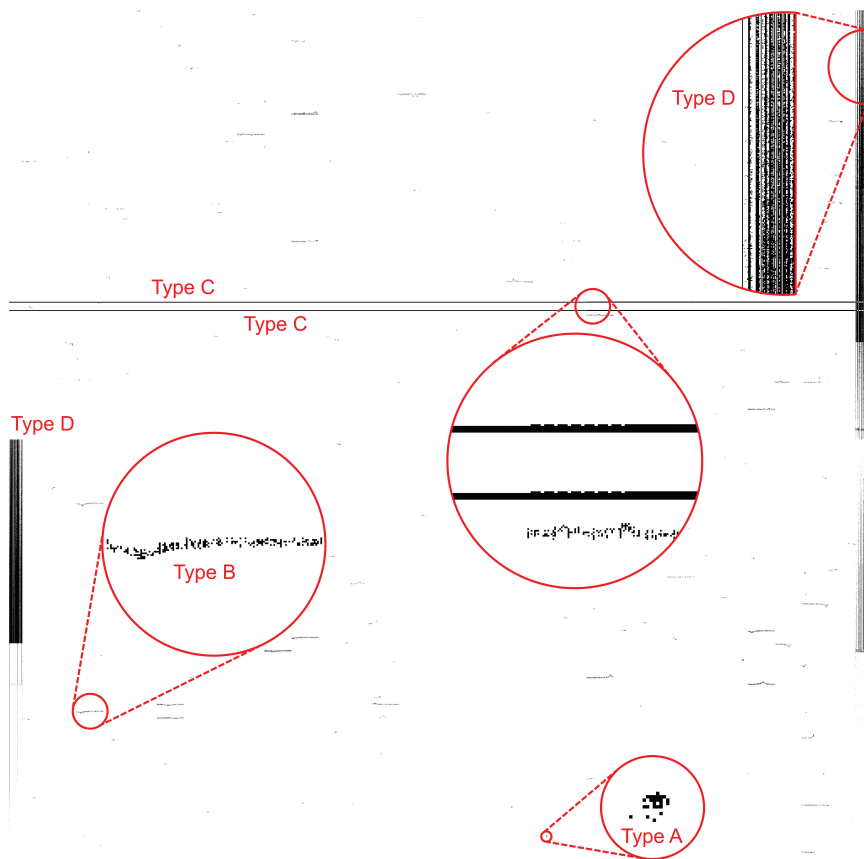


**Figure 1.23** Example of a bitmap obtained by the irradiation of a 90 nm SRAM with heavy ions. Each pixel corresponds to a bit in the memory array, and every black pixel represents a corrupted bit. The image is 4096 × 4096 pixels.

it is possible to systematically group together neighbouring upsets in clusters. Counting the clusters provides an accurate estimate of the number of single events that occurred during irradiation.

## 1.6 Conclusion

In this chapter, we introduced some elements to explain the importance of the characterization of radiation effects on electronic devices, and in particular on memories. Moreover, basic concepts such as single-event effects, total

ionizing dose effects and fault mechanisms have been introduced, in order to ease the understanding of the following chapters.

## References

- [1] ACE Science Team, “ACE Level 2 Data.”
- [2] D. H. Hathaway, “NASA/Marshall Solar Physics.”
- [3] E. C. Stone, A. M. Frandsen, R. A. Mewaldt, E. R. Christian, D. Margolies, J. F. Ormes, and F. Snow, “The Advanced Composition Explorer,” *Space Sci. Rev.*, vol. 86, no. 1/4, pp. 1–22, 1998.
- [4] A. Javanainen, “Particle radiation in microelectronics,” University of Jyväskylä, 2012.
- [5] J. R. Jokipii, C. P. Sonett, and M. S. Giampapa, *Cosmic winds and the heliosphere*. University of Arizona Press, 1997.
- [6] E. C. Stone, C. M. S. Cohen, W. R. Cook, A. C. Cummings, B. Gauld, B. Kecman, R. A. Leske, R. A. Mewaldt, M. R. Thayer, B. L. Dougherty, R. L. Grumm, B. D. Milliken, R. G. Radocinski, M. E. Wiedenbeck, E. R. Christian, S. Shuman, and T. T. von Rosenvinge, “The Solar Isotope Spectrometer for the Advanced Composition Explorer,” *Space Sci. Rev.*, vol. 86, no. 1/4, pp. 357–408, 1998.
- [7] J. A. Van Allen, C. E. McIlwain, and G. H. Ludwig, “Radiation observations with satellite 1958?”, *J. Geophys. Res.*, vol. 64, no. 3, pp. 271–286, Mar. 1959.
- [8] British Geological Survey - Natural Environment Research Council, “Magnetic Poles.”
- [9] SPENVIS Collaboration, “The Space Environment Information System”.
- [10] The CREME Collaboration, “CREME-MC site.”
- [11] A. Viljanen and R. Pirjola, “Geomagnetically induced currents in the Finnish high-voltage power system,” *Surv. Geophys.*, vol. 15, no. 4, pp. 383–408, Jul. 1994.
- [12] V. F. Hess, “Über Beobachtungen der durchdringenden Strahlung bei sieben Freiballonfahrten,” *Phys. Z.*, vol. 13, pp. 1084–1091, 1912.
- [13] J. F. Ziegler and W. A. Lanford, “Effect of Cosmic Rays on Computer Memories,” *Science (80-)*, vol. 206, no. 4420, pp. 776–788, Nov. 1979.
- [14] E. Normand, “Single event upset at ground level,” *IEEE Trans. Nucl. Sci.*, vol. 43, no. 6, pp. 2742–2750, 1996.

- [15] T. C. May and M. H. Woods, "Alpha-particle-induced soft errors in dynamic memories," *IEEE Trans. Electron Devices*, vol. 26, no. 1, pp. 2–9, Jan. 1979.
- [16] J. F. Ziegler, H. W. Curtis, H. P. Muhlfeld, C. J. Montrose, B. Chin, M. Nicewicz, C. A. Russell, W. Y. Wang, L. B. Freeman, P. Hosier, L. E. LaFave, J. L. Walsh, J. M. Orro, G. J. Unger, J. M. Ross, T. J. O'Gorman, B. Messina, T. D. Sullivan, A. J. Sykes, H. Yourke, T. A. Enger, V. Tolat, T. S. Scott, A. H. Taber, R. J. Sussman, W. A. Klein, and C. W. Wahaus, "IBM experiments in soft fails in computer electronics (1978–1994)," *IBM J. Res. Dev.*, vol. 40, no. 1, pp. 3–18, Jan. 1996.
- [17] E. Ibe, H. Taniguchi, Y. Yahagi, K. Shimbo, and T. Toba, "Impact of Scaling on Neutron-Induced Soft Error in SRAMs From a 250 nm to a 22 nm Design Rule," *IEEE Trans. Electron Devices*, vol. 57, no. 7, pp. 1527–1538, Jul. 2010.
- [18] M. Mason, "Cosmic rays damage automotive electronics." May-2006.
- [19] L. Dominik, E. Normand, M. J. Dion, and P. Ferguson, "Proposal for a new integrated circuit and electronics neutron experiment source at oak ridge national laboratory," in *2009 IEEE International Reliability Physics Symposium*, 2009, pp. 940–947.
- [20] Bloomberg, "Delta, Qantas, Air Canada Divert Flights Due to Solar Storm," Jan-2012.
- [21] E. Normand, "Single-event effects in avionics," *IEEE Trans. Nucl. Sci.*, vol. 43, no. 2, pp. 461–474, Apr. 1996.
- [22] "The IEE Seminar on Cosmic Radiation Single Event Effects and Avionics, 2005 (Ref. No. 2005/11270)," 2005, p. 0\_1.
- [23] P. K. F. Grieder, *Cosmic rays at Earth: researcher's reference manual and data book*. Elsevier Science Ltd., 2001.
- [24] B. D. Sierawski, M. H. Mendenhall, R. A. Reed, M. A. Clemens, R. A. Weller, R. D. Schrimpf, E. W. Blackmore, M. Trinczek, B. Hitti, J. A. Pellish, R. C. Baumann, S.-J. Wen, R. Wong, and N. Tam, "Muon-Induced Single Event Upsets in Deep-Submicron Technology," *IEEE Trans. Nucl. Sci.*, vol. 57, no. 6, pp. 3273–3278, Dec. 2010.
- [25] A. Hillier, K. Ishida, A. Bosser, and L. Dilillo, "Improving the Stability of Electronic Systems – Measuring the Effects of Muons on Static Random Access Memory," *Proceedings of the 14th International Conference on Muon Spin Rotation, Relaxation and Resonance*, Sapporo, Japan, 2017.

- [26] A. Bosser, “Single-Event Effects of Space and Atmospheric Radiation on Memory Components”, Doctoral dissertation, University of Jyväskylä/University of Montpellier, 2017.
- [27] J. C. Kotz, P. Treichel, and J. R. Townsend, Chemistry and chemical reactivity, 7th ed. Thomson Brooks/Cole, 2009.
- [28] G. A. Sai-Halasz, M. R. Wordeman, and R. H. Dennard, “Alpha-particle-induced soft error rate in VLSI circuits,” IEEE Trans. Electron Devices, vol. 29, no. 4, pp. 725–731, Apr. 1982.
- [29] K. Itoh, R. Hori, H. Masuda, Y. Kamigaki, H. Kawamoto, and H. Katto, “A single 5V 64K dynamic RAM,” in 1980 IEEE International Solid-State Circuits Conference. Digest of Technical Papers, 1980, vol. XXIII, pp. 228–229.
- [30] S. Martinie, J. L. Autran, S. Uznanski, P. Roche, G. Gasiot, D. Munteanu, and S. Sauze, “Alpha-Particle Induced Soft-Error Rate in CMOS 130 nm SRAM,” IEEE Trans. Nucl. Sci., vol. 58, no. 3, pp. 1086–1092, Jun. 2011.
- [31] R. Wong, P. Su, S.-J. Wen, B. Dwyer McNally, and S. Coleman, “The effect of Radon on soft error rates for wire bonded memories,” in 2010 IEEE International Integrated Reliability Workshop Final Report, 2010, pp. 133–134.
- [32] I. Batkin, R. B. del Re, J.-G. Boutin, and J. Armitage, “Gamma-spectroscopy investigation of radon daughter deposition on electrostatically charged surfaces,” Phys. Med. Biol., vol. 43, no. 3, pp. 487–499, Mar. 1998.
- [33] E. Segrè, “Fermi and Neutron Physics,” Rev. Mod. Phys., vol. 27, no. 3, pp. 257–263, 1955.
- [34] R. C. Baumann and E. B. Smith, “Neutron-induced  $^{10}\text{B}$  fission as a major source of soft errors in high density SRAMs,” Microelectron. Reliab., vol. 41, no. 2, pp. 211–218, Feb. 2001.
- [35] L. Berkhouse, S. E. Davis, F. R. Gladeck, J. H. Hallowell, and C. B. Jones, “Operation DOMINIC I-1962,” Feb. 1983.
- [36] S. L. Simon and W. L. Robison, “A compilation of nuclear weapons test detonation data for US Pacific Ocean tests,” Heal. Phys., vol. 73, no. 1, pp. 258–264, 1997.
- [37] P. Sigmund, Stopping of heavy ions : a theoretical approach. Springer, 2004.
- [38] P. Sigmund, “Stopping Power: Wrong Terminology,” ICRU News, 2000.

- [39] P. Sigmund, Particle Penetration and Radiation Effects – General Aspects and Stopping of Swift Point Charges. Springer, 2006.
- [40] N. Bohr, “On the theory of the decrease of velocity of moving electrified particles on passing through matter,” *Philos. Mag. Ser. 6*, vol. 25, no. 145, pp. 10–31, 1913.
- [41] N. Bohr, “On the decrease of velocity of swiftly moving electrified particles in passing through matter,” *Philos. Mag. Ser. 6*, vol. 30, no. 178, pp. 581–612, 1915.
- [42] N. Bohr, “The penetration of atomic particles through matter,” *Kgl. Danske Vidensk. Selsk. Mat.-Fys. Medd.*, vol. 18, no. 8, pp. 1–144, 1948.
- [43] J. Lindhard and A. H. Sorensen, “Relativistic theory of stopping for heavy ions,” *Phys. Rev. A*, vol. 53, no. 4, pp. 2443–2456, 1996.
- [44] F. Yang and J. H. Hamilton, Modern Atomic and Nuclear Physics. World Scientific Pub Co., 2009.
- [45] J. Lilley, Nuclear Physics - Principles and Applications. John Wiley & Sons Ltd., 2001.
- [46] P. E. Dodd, J. R. Schwank, M. R. Shaneyfelt, V. Ferlet-Cavrois, P. Paillet, J. Baggio, G. L. Hash, J. A. Felix, K. Hirose, and H. Saito, “Heavy Ion Energy Effects in CMOS SRAMs,” *IEEE Trans. Nucl. Sci.*, vol. 54, no. 4, pp. 889–893, Aug. 2007.
- [47] Y. P. Varshni, “Temperature dependence of the energy gap in semiconductors,” *Physica*, vol. 34, no. 1, pp. 149–154, Jan. 1967.
- [48] T. H. DiStefano and D. E. Eastman, “The band edge of amorphous SiO<sub>2</sub> by photoinjection and photoconductivity measurements,” *Solid State Commun.*, vol. 9, no. 24, pp. 2259–2261, Dec. 1971.
- [49] R. C. Alig and S. Bloom, “Electron-Hole-Pair Creation Energies in Semiconductors,” *Phys. Rev. Lett.*, vol. 35, no. 22, pp. 1522–1525, Dec. 1975.
- [50] J. M. Benedetto and H. E. Boesch, “The Relationship between 60Co and 10-keV X-Ray Damage in MOS Devices,” *IEEE Trans. Nucl. Sci.*, vol. 33, no. 6, pp. 1317–1323, 1986.
- [51] R. Harboe-Sorensen, C. Poivey, F.-X. Guerre, A. Roseng, F. Lochon, G. Berger, W. Hajdas, A. Virtanen, H. Kettunen, and S. Duzellier, “From the Reference SEU Monitor to the Technology Demonstration Module On-Board PROBA-II,” *IEEE Trans. Nucl. Sci.*, vol. 55, no. 6, pp. 3082–3087, Dec. 2008.
- [52] R. Harboe-Sorensen, F.-X. Guerre, and A. Roseng, “Design, Testing and Calibration of a ‘Reference SEU Monitor’ System,” in 2005 8th

- European Conference on Radiation and Its Effects on Components and Systems, 2005, pp. B3-1-B3-7.
- [53] G. C. Messenger and M. S. Ash, Single event phenomena. Chapman & Hall, 1997.
  - [54] M. A. Xapsos, "A Spatially Restricted Linear Energy Transfer Equation," *Radiat. Res.*, vol. 132, no. 3, p. 282, Dec. 1992.
  - [55] M. A. Xapsos, "Applicability of LET to single events in micro-electronic structures," *IEEE Trans. Nucl. Sci.*, vol. 39, no. 6, pp. 1613–1621, 1992.
  - [56] M. Xapsos, G. Summers, E. Burke, and C. Poivey, "Microdosimetry theory for microelectronics applications," *Nucl. Instruments Methods Phys. Res. Sect. B Beam Interact. with Mater. Atoms*, vol. 184, no. 1–2, pp. 113–134, Sep. 2001.
  - [57] J. J. Butts and R. Katz, "Theory of RBE for Heavy Ion Bombardment of Dry Enzymes and Viruses," *Radiat. Res.*, vol. 30, no. 4, pp. 855–871, Apr. 1967.
  - [58] R. Katz, "Track structure theory in radiobiology and in radiation detection," *Nucl. Track Detect.*, vol. 2, no. 1, pp. 1–28, Mar. 1978.
  - [59] F. A. Cucinotta, R. Katz, and J. W. Wilson, "Radial distribution of electron spectra from high-energy ions," *Radiat. Environ. Biophys.*, vol. 37, no. 4, pp. 259–265, Dec. 1998.
  - [60] B. Grosswendt, S. Pszona, and A. Bantsar, "New descriptors of radiation quality based on nanodosimetry, a first approach," *Radiat. Prot. Dosimetry*, vol. 126, no. 1–4, pp. 432–444, May 2007.
  - [61] K. M. Prise, G. Schettino, M. Folkard, and K. D. Held, "New insights on cell death from radiation exposure," *Lancet Oncol.*, vol. 6, no. 7, pp. 520–528, Jul. 2005.
  - [62] "The International Technology Roadmap for Semiconductors."
  - [63] Intel, "Microprocessor Quick Reference Guide."
  - [64] J. F. Ziegler, J. P. Biersack, M. Ziegler, D. J. Marwick, G. A. Cuomo, W. A. Porter, and S. A. Harrison, "{SRIM} 2013 code," vol. SRIM-2013.
  - [65] V. Zajic, "TVDG LET Calculator," vol. 1.24. 2001.
  - [66] V. Zajic and P. Thieberger, "Heavy ion linear energy transfer measurements during single event upset testing of electronic devices," *IEEE Trans. Nucl. Sci.*, vol. 46, no. 1, pp. 59–69, Feb. 1999.
  - [67] A. Javanainen, W.~H.~Trzaska, R.~Harboe-Sørensen, A. Virtanen, G.~Berger, and W.~Hajdas, "ECIF Cocktail Calculator."

- [68] A. Javanainen, “A simple expression for electronic stopping force of heavy ions in solids,” *Nucl. Instruments Methods Phys. Res. Sect. B Beam Interact. with Mater. Atoms*, vol. 285, pp. 158–161, Aug. 2012.
- [69] P. Sigmund, “{PASS} code.”
- [70] P. Sigmund and A. Schinner, “Binary theory of electronic stopping,” *Nucl. Instruments Methods Phys. Res. Sect. B Beam Interact. with Mater. Atoms*, vol. 195, no. 1–2, pp. 64–90, Oct. 2002.
- [71] G. Schiwietz and P. L. Grande, “Convolution approximation for swift Particles.”
- [72] P. Helmut, “Stopping Power of Matter for Ions.”
- [73] F. Hubert, R. Bimbot, and H. Gauvin, “Range and stopping-power tables for 2.5–500 MeV/nucleon heavy ions in solids,” *At. Data Nucl. Data Tables*, vol. 46, no. 1, pp. 1–213, Sep. 1990.
- [74] Geant4 Collaboration, “Geant4: A toolkit for the simulation of the passage of particles through matter.”
- [75] A. Javanainen, T. Malkiewicz, J. Perkowski, W. H. Trzaska, A. Virtanen, G. Berger, W. Hajdas, R. Harboe-Sørensen, H. Kettunen, V. Lyapin, M. Mutterer, A. Pirojenko, I. Riihimäki, T. Sajavaara, G. Tyurin, and H. J. Whitlow, “Linear energy transfer of heavy ions in silicon,” *IEEE Trans. Nucl. Sci.*, vol. 54, no. 4, pp. 1158–1162, Aug. 2007.
- [76] T. R. Oldham and F. B. McLean, “Total ionizing dose effects in MOS oxides and devices,” *IEEE Trans. Nucl. Sci.*, vol. 50, no. 3, pp. 483–499, Jun. 2003.
- [77] R. L. Pease, “Total ionizing dose effects in bipolar devices and circuits,” *IEEE Trans. Nucl. Sci.*, vol. 50, no. 3, pp. 539–551, Jun. 2003.
- [78] “Test Procedures for the Measurement of Single-Event Effects in Semiconductor Devices from Heavy Ion Irradiation.” 1996.
- [79] “Measurement and Reporting of Alpha Particle and Terrestrial Cosmic Ray-Induced Soft Errors in Semiconductor Devices.” 2006.
- [80] P. C. Adell, R. D. Schrimpf, C. R. Cirba, W. T. Holman, X. Zhu, H. J. Barnaby, and O. Mion, “Single event transient effects in a voltage reference,” *Microelectron. Reliab.*, vol. 45, no. 2, pp. 355–359, Feb. 2005.
- [81] N. D. P. Avirneni and A. Somani, “Low Overhead Soft Error Mitigation Techniques for High-Performance and Aggressive Designs,” *IEEE Trans. Comput.*, vol. 61, no. 4, pp. 488–501, Apr. 2012.

- [82] M. Nicolaidis, Soft Errors in Modern Electronic Systems. Springer, 2010.
- [83] F. W. Sexton, “Destructive single-event effects in semiconductor devices and ICs,” IEEE Trans. Nucl. Sci., vol. 50, no. 3, pp. 603–621, Jun. 2003.
- [84] J. R. Schwank, V. Ferlet-Cavrois, M. R. Shaneyfelt, P. Paillet, and P. E. Dodd, “Radiation effects in SOI technologies,” IEEE Trans. Nucl. Sci., vol. 50, no. 3, pp. 522–538, Jun. 2003.
- [85] A. Bosio, L. Dilillo, P. Girard, S. Pravossoudovitch, and A. Virazel, “Advanced Test Methods for SRAMs – Effective Solutions for Dynamic Fault Detection in Nanoscaled Technologies.” Springer, 2010.
- [86] F. Wrobel, J.-M. Palau, M. “Induced nuclear reactions in a simplified SRAM structure: scaling effects on SEU and MBU” IEEE Trans. Nucl. Sci., vol. 48, no. 6, pp. 1946–1952, Dec. 2001.
- [87] R. C. Baumann “radiation induced soft errors in advanced semiconductor technologies”, IEEE Trans. Device Mater. Reliab., vol. 5, no. 3, pp. 305–316, Sep. 2005.
- [88] T. Heijmen et al. “Factors that impact the critical charge of memory elements”, in proc. IOLTS 2006, pp. 57–62.
- [89] “Space Product Assurance - Commercial electrical, electronic and electromechanical (EEE) components.” ECSS-Q-ST-60-13C, 21-Oct-2013.] [JESD89, “Measurement and reporting of alpha particles and terrestrial cosmic ray induced Soft Error in Semiconductor devices.” JEDEC Standard.
- [90] “Test Procedures for the Measurement of Single-Event Effects in Semiconductor Devices from Heavy Ion Irradiation.” JEDEC Test Standard, No 57, Dec-1996.
- [91] D. Radaelli, H. Puchner, S. Wong, and S. Daniel, Investigation of multi-bit upsets in a 150 nm technology SRAM device, IEEE Trans. Nucl. Sci., vol. 52, no. 6, pp. 2433–2437, Dec. 2005.
- [92] P. Rech, J.-M. Galliere, P. Girard, A. Griffoni, J. Boch, F. Wrobel, F. Saigne, and L. Dilillo, “Neutron-Induced Multiple Bit Upsets on Two Commercial SRAMs Under Dynamic-Stress,” IEEE Trans. Nucl. Sci., vol. 59, no. 4, pp. 893–899, Aug. 2012.
- [93] V. Gupta, A. Bosser, G. Tsiligiannis, A. Zadeh, A. Javanainen, A. Virtanen, H. Puchner, F. Saigné, F. Wrobel and L. Dilillo, “Heavy-ion radiation impact on a 4Mb FRAM under different test conditions”,

- European Conference on Radiation and its Effects on Components and Systems (RADECS), Moscow, Russia, Sept. 2015.
- [94] L. Dilillo, G. Tsiligiannis, V. Gupta, A. Bosser, F. Saigné and F. Wrobel, "Soft errors in commercial off-the-shelf static random access memories", Journal of Semiconductor Science and Technology, vol 32, I 1, DOI: 10.1088/1361-6641/32/1/013006, 2016.
  - [95] "Single Event Effects Test Method and Guidelines," ESCC Basic Specif. No. 25100, 2002.
  - [96] "Total Dose Steady-State Irradiation Test Method." Oct-2010.
  - [97] "Test Method Standard-Microcircuits." 2010.
  - [98] "Standard Guide for the Measurement of Single Event Phenomena (SEP) Induced by Heavy Ion Irradiation of Semiconductor Devices." 2006.
  - [99] A. J. Tylka, J. H. Adams, P. R. Boberg, B. Brownstein, W. F. Dietrich, E. O. Flueckiger, E. L. Petersen, M. A. Shea, D. F. Smart, and E. C. Smith, "CREME96: a revision of the Cosmic Ray Effects on Micro-Electronics code," IEEE Trans. Nucl. Sci., vol. 44, no. 6, pp. 2150–2160, 1997.
  - [100] International Atomic Energy Agency – Nuclear Data Service, "Live Chart of Nuclides".
  - [101] G. Berger, "Heavy Ion Irradiation Facility (HIF)." 2004.
  - [102] A. Virtanen, H. Kettunen, A. Javanainen, M. Rossi, and J. Jaatinen, "RADiation Effects Facility at JYFL".
  - [103] "Radiation Effects Facility/The Cyclotron Institute/Texas A&M University".
  - [104] R. Harboe-Sorensen, C. Poivey, A. Zadeh, A. Keating, N. Fleurinck, K. Puimege, F.-X. Guerre, F. Lochon, M. Kaddour, L. Li, and D. Walter, "PROBA-II Technology Demonstration Module In-Flight Data Analysis," IEEE Trans. Nucl. Sci., vol. 59, no. 4, pp. 1086–1091, Aug. 2012.
  - [105] European Space Components Coordination, "Total Dose Steady-State Irradiation Test Method – ESCC Basic Specification No. 22900," 2010.
  - [106] D. M. Fleetwood, S. L. Kosier, R. N. Nowlin, R. D. Schrimpf, R. A. Reber, M. DeLaus, P. S. Winokur, A. Wei, W. E. Combs, and R. L. Pease, "Physical mechanisms contributing to enhanced bipolar gain degradation at low dose rates," IEEE Trans. Nucl. Sci., vol. 41, no. 6, pp. 1871–1883, Dec. 1994.
  - [107] I. Jun, M. A. Xapsos, S. R. Messenger, E. A. Burke, R. J. Walters, G. P. Summers, and T. Jordan, "Proton Nonionizing Energy Loss (NIEL) for

- Device Applications,” in IEEE Transactions on Nuclear Science, 2003, vol. 50, no. 6 I, pp. 1924–1928.
- [108] S. R. Messenger, E. A. Burke, M. A. Xapsos, G. P. Summers, R. J. Walters, I. Jun, and T. Jordan, “NIEL for Heavy Ions: An Analytical Approach,” in IEEE Transactions on Nuclear Science, 2003, vol. 50, no. 6 I, pp. 1919–1923.
- [109] University of Jyväskylä, “RADEF – Radiation Effects Facility.” [Online]. Available: <https://www.jyu.fi/science/en/physics/research/infrastructures/accelerator-laboratory/radiation-effects-facility>. [Accessed: 13-Mar-2018].
- [110] Paul Scherrer Institute, “PIF webpage.” [Online]. Available: <https://www.psi.ch/pif/>. [Accessed: 13-Mar-2018].
- [111] R. Ladbury, R. A. Reed, P. Marshall, K. A. LaBel, R. Anantaraman, R. Fox, D. P. Sanderson, A. Stoltz, J. Yurkon, A. F. Zeller, and J. W. Stetson, “Performance of the high-energy single-event effects test Facility (SEETF) at Michigan State university’s national Superconducting Cyclotron laboratory (NSCL),” IEEE Trans. Nucl. Sci., vol. 51, no. 6, pp. 3664–3668, Dec. 2004.
- [112] B. W. Riemer, F. X. Gallmeier, and L. J. Dominik, “Single Event Effects test facility at Oak Ridge National Laboratory,” in 2015 IEEE/AIAA 34th Digital Avionics Systems Conference (DASC), 2015, p. 8C6-1-8C6-12.
- [113] G. Tsiliogiannis, L. Dilillo, A. Bosio, P. Girard, S. Pravossoudovitch, A. Todri-Sanial, A. Virazel, H. Puchner, C. Frost, F. Wrobel and F. Saigné, “Multiple-Cell-Upsets Classification in commercial SRAMs,” IEEE Transaction on Nuclear Science, DOI 10.1109/TNS.2014.2313742, 2014.